

Orbital-resolved DFT+U for molecules and solids

Eric Macke,^{*,†} Iurii Timrov,^{‡,§} Nicola Marzari,^{‡,¶} and Lucio Colombi Ciacchi[†]

[†]*Faculty of Production Engineering, Bremen Center for Computational Materials Science and MAPEX Center for Materials and Processes, Hybrid Materials Interfaces Group, University of Bremen, Am Fallturm 1, 28359 Bremen, Germany*

[‡]*Theory and Simulation of Materials (THEOS) and National Centre for Computational Design and Discovery of Novel Materials (MARVEL), École Polytechnique Fédérale de Lausanne, CH-1015 Lausanne, Switzerland*

[¶]*University of Bremen Excellence Chair, Bremen Center for Computational Materials Science*

[§]*Present address: Laboratory for Materials Simulations (LMS), Paul Scherrer Institut (PSI), CH-5232 Villigen PSI, Switzerland*

E-mail: emacke@uni-bremen.de

Abstract

We present an orbital-resolved extension of the Hubbard U correction to density-functional theory (DFT). Compared to the conventional shell-averaged approach, the prediction of energetic, electronic and structural properties is strongly improved, particularly for compounds characterized by both localized and hybridized states in the Hubbard manifold. The numerical values of all Hubbard parameters are readily obtained from linear-response calculations. The relevance of this more refined approach is showcased by its application to bulk solids pyrite (FeS_2) and pyrolusite ($\beta\text{-MnO}_2$), as well as to six Fe(II) molecular complexes. Our findings indicate that a careful definition of Hubbard manifolds is indispensable for extending the applicability of DFT+ U

beyond its current boundaries. The present orbital-resolved scheme aims to provide a computationally undemanding yet accurate tool for electronic structure calculations of charge-transfer insulators, transition-metal (TM) complexes and other compounds displaying significant orbital hybridization.

1 Introduction

Hubbard corrections are among the most widely used improvements to approximate Kohn-Sham (KS) density-functional theory (DFT).^{1,2} The combination of DFT with the Hubbard model,³ referred to as DFT+ U , was inspired by this widely studied model of electron correlations and introduced to improve the description provided by local or semi-local exchange-correlation (xc) functionals, such as the local-density approximation (LDA) and the generalized-gradient approximation (GGA), for the case of Mott-Hubbard insulators⁴⁻⁶ or more broadly strongly correlated electrons.

It was recognized early on^{7,8} that a simplified, rotationally invariant formulation of DFT+ U ⁹ provided a natural connection to the requirement of piecewise linearity of the exact energy functional:^{10,11} the Hubbard correction of Dudarev effectively removes the non-linear (almost quadratic) behavior of the total energy with respect to the occupation of the Hubbard manifold, and replaces it with a linear term. In this light, the strength of the U parameter can be determined fully from first principles, and obtained from the second derivative of the energy (once the non-interacting terms are removed) with respect to the occupations,^{7,8} so that the quadratic curvature is removed by DFT+ U . This connection is heuristic, and relies on the (very reasonable) assumption that the localized electrons in the d or f manifold are only weakly interacting with the rest of the electron bath, so that this manifold also follows the condition of piecewise linearity (PWL) that is in principle valid only for the total energy functional.¹⁰ The overstabilization of fractional occupations in standard (semi)-local functionals is driven by the incomplete cancellation from the xc functional to the Hartree term (cancellation that is exact instead in Hartree-Fock), leading

to a strong (one-electron) self-interaction component. This is particularly severe for localized electrons, that over-delocalize and over-hybridize with their ligands. So, the DFT+ U correction should be seen as a self-interaction correction, providing an approximate screened Fock-like contribution; this was stated early on, highlighting how even for molecular systems containing only one site (i.e., one TM atom) the electronic-structure description provided by DFT+ U is greatly improved, both qualitatively and quantitatively.¹² In other words, while the original Hubbard model was concerned with the correlation effects that appear on a lattice, where each site can only contain 0, 1 or 2 electrons, the functional form that the model inspires, once applied to the continuum of the electron gas of approximate DFT, does not any more account for correlations between sites, but counteracts the tendency of strongly localized electrons to hybridize with their ligands, driven by incomplete cancellation in the Hartree term of the one-electron self-interaction. This can be easily argued not only by applying DFT+ U to molecules,¹² but also by the simple observation that changing the value of U changes the charge transfer to/from the ligands,¹³ but does not transfer charge to the Hubbard manifolds on the other sites, highlighting the completely different physics of the Hubbard Hamiltonian on a lattice, and the Hubbard U correction in the continuum of Kohn-Sham electrons. Incidentally, strongly correlated materials have almost invariably very localized d or f electrons, so do benefit from DFT+ U – but not because the latter improves the treatment of correlations, but just because it decreases the self-interaction errors (SIE). It is important to iterate that PWL is a property that a system must obey on the *global* scale, i.e., with respect to the changes in the total number of electrons.¹⁴ DFT+ U , on the other hand, seeks to eliminate the curvature *locally* by restoring the piece-wise linear behavior in a subspace known as the Hubbard manifold.^{8,15} The relation between self-interaction and piecewise linearity in many-electron systems is somewhat confusing; in fact, Koopmans functionals^{16,17} impose (very accurately) piecewise linearity on each orbital in a given system, but do not correct self-interaction; the integer Koopmans functional (KI) provides the same exact total energy of the base functional (LDA or GGA), but a completely different

spectrum.

A key challenge in DFT+ U arises from the (*a priori*) choice of the value of the on-site Hubbard U parameter. Often, U is considered a tunable quantity, adjusted to achieve agreement with experimental results for specific properties of interest such as band gaps, lattice parameters, magnetic moments, or formation enthalpies.^{18–21} However, this empirical procedure possesses limited predictive capabilities due to its reliance on experimental data; not to mention that certain quantities, like band gaps, are not even meant to be predicted by DFT. Alternatively, U values can be computed from first principles. The different methods that have been proposed for this purpose can be classified into three groups: the constrained DFT approach (cDFT),^{22–30} the constrained random phase approximation (cRPA),^{31–35} and Hartree-Fock based approaches.^{36–41} The linear-response formulation of constrained DFT (LR-cDFT)⁸ has become a method of choice for many DFT+ U studies.^{42–50} A recent reformulation of this method in terms of density-functional perturbation theory (DFPT)^{51,52} has significantly enhanced its success. This reformulation enables the replacement of computationally expensive supercells with primitive unit cells, utilizing monochromatic perturbations. As a result, the computational burden of determining Hubbard parameters is substantially reduced.

As evident from the large variety of available methods, considerable attention has been devoted to the numerical evaluation of U for a given manifold. However, the question how this manifold must be defined, that is, *which* electronic states require on-site Hubbard corrections, is a critical yet often overlooked aspect in DFT+ U . Recalling that the main motivation of Hubbard U corrections lies in the mitigation of local SIE through recovery of PWL of the total energy, the Hubbard manifold should contain those and only those states that substantially contribute to the former. Oftentimes, self-interaction occurs in partially occupied d and f shells due to their high electron count and localization; hence, these are the traditional targets of Hubbard U corrections. Nevertheless, self-interaction can also manifest itself in s and p shells, and even in localized molecular orbitals (MO).⁵³ Moreover,

the definition of the Hubbard manifold also involves choosing so-called Hubbard-projector functions that suitably represent the states to be corrected (details follow in Section 2.2). In fact, it has been shown that the choice of the projector function can have a stronger impact on the calculation than the numerical value of U , especially when orbital overlap is appreciable.^{45,54,55} Therefore, it is essential to choose a U value that is consistent with the projectors used (see appendix of Ref. 56).

The significance of judiciously selecting the Hubbard manifold becomes particularly evident in the context of optical properties. Although DFT is a total energy theory and KS orbitals have no direct physical meaning except for the highest occupied molecular orbital (HOMO), KS eigenvalues are commonly used as estimates for experimental quasiparticle energies. Unfortunately, uncorrected (semi-)local DFT functionals tend to severely underestimate properties such as band gaps and ionization energies; a fact that has been linked to deviations from PWL.^{16,17,57} Thus, Koopmans-compliant functionals^{16,17,58} systematically improve spectral properties by imposing PWL on all orbitals in the system. For example, a recent study by [Nguyen et al.](#) found an average band gap error of only 0.22 eV for a test set of 30 semiconductors.⁵⁹ Conversely, DFT+ U can only achieve such improvements if the Hubbard manifold sufficiently overlaps with the frontier orbitals.^{15,45,60} This might explain why DFT+ U has been successfully applied to many Mott-Hubbard insulators, while its predictive capabilities are less reliable when applied to charge-transfer (CT) insulators. While in the former both the valence band maximum (VBM) and the conduction band minimum (CBM) primarily consist of localized TM d states, the frontier states of the latter possess significant ligand orbital character. In this case, the sole correction of TM d shells does not necessarily target all major sources of SIE. Additionally, the representation of the hybridized orbitals through atomic-like Hubbard projectors can be deceptive.

Some authors have explored including ligand orbitals in the on-site Hubbard manifold, for example applying U corrections to oxygen and S- p shells of TM oxides, perovskites and sulfides.^{45,48,61–63} The extended DFT+ U + V framework⁵³ was adopted for scenarios where

hybridization plays an eminent role. This method augments DFT+ U by an inter-site Hubbard V term, and so acts on combinations of projectors located on different sites, enhancing accuracy and transferability.^{41,54,64–73} Finally, many open-shell systems require unlike-spin terms such as Hund’s J . In DFT+ $U+J$, these terms introduce anisotropy in the Hubbard correction with respect to the spin channels, while also reducing the effective value of the U parameter.^{48,60,62,74,75} On the other hand, it is unlikely that multi-reference configurations, as common in open-shell systems, might be described well with any + U or $U+J$ correction.

What is striking about the aforementioned approaches is that the d shell Hubbard manifold is either *extended* by additional states (U on ligands or V on molecular orbitals) or internally *rebalanced* (DFT+ $U+J$). But what if the practice of including the entire d shell is, in itself, problematic? Recent work by [Mariano et al.](#) suggests that this might indeed occur in some cases. Their study revealed that applying U corrections to the d shells of Fe in strong-field Fe(II) hexacomplexes leads to a spurious suppression of LS states due to what appears to be an over-correction of hybridized e_g orbitals.^{76,77} Furthermore, the use of *ab initio* Hubbard U parameters derived from LR-cDFT led to a significant decrease in the overall accuracy of the spin-state energies when compared to empirical U values. These and other observations suggest a critical analysis of the current practice of how (shell-averaged) Hubbard U corrections are applied to DFT. After all, the correction of all magnetic quantum orbitals within a given shell using the same scalar U parameter is inherently a simplistic approximation.⁷⁸

Therefore, it is worthwhile to investigate whether departing from the shell-averaged approximation can improve DFT+ U calculations concerning energetic, structural, and magnetic properties. This possibility has been explored in a few works. For example, [Solovyev et al.](#) showed that a selective application of U corrections to the t_{2g} manifolds of LaMO_3 perovskites ($M=\text{Ti}-\text{Cu}$) significantly improves the agreement of band gaps and magnetic orderings with experiments compared to both uncorrected LDA and shell-averaged LDA+ U .⁷⁹ The authors argue that e_g electrons are reasonably described by the uncorrected LDA func-

tional because of their “itinerant“ behavior that arises due to the strong σ overlap between O-2*p* and M-*e_g* orbitals. Pickett et al. adopted the cDFT approach to compute the Hubbard parameters of Fe in bulk FeO as a matrix (**U**) with *U* values specific to the *t_{2g}* and *e_g* manifolds, respectively.²⁷ Using a different scheme, orbital-resolved Hubbard parameters were obtained by mapping shell-averaged *U* and *J* parameters onto orbital-dependent interaction and exchange matrices $U_{mm'}$ and $J_{mm'}$ using atomic Slater integrals and Gaunt’s numbers.^{80–83} Other works focused on the spin-dependence of *U*, finding that the spin-resolved on-site parameters can be pivotal for a physical description of magnetic systems.^{49,50,84}

Despite these early efforts, orbital-resolved Hubbard *U* parameters have not gained widespread use in the DFT community. This is surprising in light of the fact that orbital-specific Hubbard manifolds are quite common in the dynamical mean-field theory (DMFT) community.^{85–88} In the latter, Hubbard *U* parameters are routinely computed for manifolds that range from groups of orbitals (e.g., *t_{2g}* models) to combinations of multiple shells localized on different atoms (e.g., *d – p* models)⁸⁶ using cRPA in conjunction with various sets of Wannier projector functions that encompass the specific manifold of interest.^{31,32} To date, only a few publicly available DFT codes incorporate this capability. For example, DFT codes that use Wannier function-based Hubbard projectors (e.g., ONETEP⁸⁹) indirectly facilitate orbital-resolved DFT+*U* calculations as the Wannier functions can be chosen to only represent the desired subset of orbitals, e.g., *t_{2g}*.⁵⁵

In this paper we present a user-friendly yet general implementation of orbital-resolved DFT+*U* that works with any kind of Hubbard projector. The numerical values of the necessary parameters are extracted from first principles using an orbital-resolved LR-cDFT approach.⁸ We benchmark the orbital-resolved scheme by carrying out calculations of bulk pyrite (FeS₂), bulk pyrolusite (β -MnO₂) and six Fe(II) molecular hexacomplexes of varying ligand strength. For all of these strongly covalent compounds, the refined approach leads to a substantial improvement in the prediction of structural and energetic properties, aligning more closely with experimental observations than conventional DFT+*U* or even DFT+*U*+*V*.

Moreover, we observe that the orbital-resolved U parameters are considerably smaller, by up to 80%, than their corresponding shell-averaged counterparts.

The remainder of the paper is organized as follows. In Section 2, we describe the transition from the customary, shell-averaged implementations of the DFT+ U energy functional and the LR-cDFT approach to their generalized, orbital-resolved forms. Subsequently, Section 3 briefly lists the relevant technical details of the calculations, whose results are presented and discussed in Section 4. Section 5 is dedicated to the relationship between the orbital-resolved (on-site) Hubbard U presented in this work and the (inter-site) V terms of Ref. 53. Finally, we summarize the main conclusions in Section 6.

2 DFT+ U : orbital-resolved Hubbard parameters

2.1 The energy functional

As this work focuses on the on-site U term of Hubbard-corrected DFT, we start from the widespread shell-averaged and rotationally-invariant formulation of DFT+ U by Dudarev et al.⁹ Written in a way that allows for the simultaneous correction of multiple subshells on the same atom, the energy functional reads:⁹⁰

$$E_{\text{DFT}+U} = E_{\text{DFT}} + E_U = E_{\text{DFT}} + \sum_{I,\sigma} \sum_{nl} \frac{U_{nl}^I}{2} \text{Tr} [\mathbf{n}_{nl}^{I\sigma} (1 - \mathbf{n}_{nl}^{I\sigma})] , \quad (1)$$

where E_{DFT} is the DFT total energy computed with standard (semi-)local xc functionals, U_{nl}^I is an effective on-site Hubbard parameter, and $\mathbf{n}_{nl}^{I\sigma}$ is the orbital occupation matrix. The summation over the principal (n) and orbital (l) quantum numbers implies that Hubbard U corrections can be applied simultaneously to multiple subshells of the same atom,^{45,53} although it usually suffices to treat the valence shell alone. For the sake of clarity, we henceforth omit the index nl , assuming that the Hubbard manifolds consist of, at most, one subshell per atom. The orbital occupation matrix defines how the Hubbard correction is

applied. For a given spin σ , its elements are computed by projecting the valence KS wave functions onto the Hubbard manifold of an atom I :

$$n_{mm'}^{I\sigma} = \sum_{\mathbf{k},\nu} f_{\mathbf{k},\nu}^{\sigma} \langle \psi_{\mathbf{k},\nu}^{\sigma} | \hat{P}_{m'm}^I | \psi_{\mathbf{k},\nu}^{\sigma} \rangle, \quad (2)$$

where m and m' are the magnetic quantum numbers of the Hubbard manifold, ν represents the band labels of the KS wave functions, \mathbf{k} indicates points in the first Brillouin zone, and $f_{\mathbf{k},\nu}^{\sigma}$ are occupations of the KS wave functions $\psi_{\mathbf{k},\nu}^{\sigma}$. If atomic-like orbitals (φ_m^I) are used as projector functions (*vide infra*), one may define $\hat{P}_{m'm}^I = |\varphi_{m'}^I\rangle\langle\varphi_m^I|$. Note, however, that if plane-wave basis sets are used, the expression of \hat{P} also depends on the type of the pseudopotential.⁵² Applying Hubbard U corrections also modifies the KS potential of the target orbitals according to

$$\hat{V}_U^{\sigma} = \sum_I U^I \sum_{mm'} \left(\frac{\delta_{mm'}}{2} - n_{mm'}^{I\sigma} \right) |\varphi_m^I\rangle\langle\varphi_{m'}^I|, \quad (3)$$

where $\delta_{mm'}$ is the Kronecker delta. It is evident from Eq. (3) that Hubbard U corrections exert a stabilizing influence on fully occupied orbitals, reducing their KS potential by up to $U/2$, while producing the opposite effect on empty orbitals.

Provided a correct normalization of the Hubbard projector functions, the eigenvalues of $n_{mm'}^{I\sigma}$ express the occupation of the $2l+1$ orbitals with numbers between 0 (fully empty) and 1 (fully occupied). They are obtained by solving the eigenvalue problem⁸

$$\mathbf{n}^{I\sigma} \mathbf{v}_i^{I\sigma} = \lambda_i^{I\sigma} \mathbf{v}_i^{I\sigma}, \quad (4)$$

where $\lambda_i^{I\sigma}$ and $\mathbf{v}_i^{I\sigma}$ are the eigenvalues and eigenvectors, respectively, and i is a dummy index running from 1 to $2l+1$. This allows us to re-write the E_U contribution of Eq. (1) more

concisely in terms of these eigenvalues:

$$E_U = \sum_{I,\sigma} \frac{U^I}{2} \sum_i^{2l+1} \lambda_i^{I\sigma} (1 - \lambda_i^{I\sigma}). \quad (5)$$

Within this diagonal representation, Eq. (5) can be readily generalized to become an orbital-resolved correction:

$$E_U = \sum_{I,\sigma} \sum_i^{2l+1} \frac{U_i^I}{2} \lambda_i^{I\sigma} (1 - \lambda_i^{I\sigma}), \quad (6)$$

Here, U_i^I is now an effective on-site Hubbard parameter specific to the i th orbital of the Hubbard manifold localized on atom I .

Similar generalizations of the shell-averaged DFT+ U functional were already postulated by [Pickett et al.](#) and used by [Solovyev et al.](#), although these early works adopted DFT+ U energy functionals different from [Dudarev et al.](#)'s formulation.

In practical calculations, not every orbital requires a distinct U_i^I , and it might suffice to distinguish between the irreducible representations that follow from local point group symmetry. For instance, considering the d shell of an octahedrally coordinated atom with local O_h point group symmetry, Eq. (6) can be written as

$$E_U = \sum_{I,\sigma} \frac{U_{t_{2g}}^I}{2} \sum_{i \in \{t_{2g}\}} \lambda_i^{I\sigma} (1 - \lambda_i^{I\sigma}) + \sum_{I,\sigma} \frac{U_{e_g}^I}{2} \sum_{i \in \{e_g\}} \lambda_i^{I\sigma} (1 - \lambda_i^{I\sigma}), \quad (7)$$

where $U_{t_{2g}}^I$ and $U_{e_g}^I$ are the Hubbard parameters for the t_{2g} and e_g orbitals, respectively, and $i \in \{t_{2g}\}$ means that i runs over the orbital indices of the t_{2g} subshell, while $i \in \{e_g\}$ means that i runs over the orbital indices of the e_g subshell. It is also possible to selectively exclude specific orbitals from receiving Hubbard corrections by setting $U_i^I = 0$.

The calculation of the Hubbard potential (Eq. (3)) is also performed in the diagonal representation by rotating the atomic-like orbitals φ_m^I from the global to the local coordinate system using the eigenvectors $\mathbf{v}_i^{I\sigma}$. However, after computing the orbital-resolved contributions to the Hubbard potential \hat{V}_U , we perform a backrotation into the non-diagonal

representation as this allows to use existing implementations of density mixing as well as the calculation of forces and stresses with no further adaption.

A crucial aspect for a successful application of Hubbard corrections lies in finding a suitable projector function for the target manifold, as this controls the occupation eigenvalues $\lambda_i^{I\sigma}$ (Eq. (2)) which govern the corrective Hubbard energy. The next subsection offers a concise introduction to the prevailing and commonly utilized approaches.

2.2 Hubbard projector functions

There are many ways to define Hubbard projector functions within the DFT+ U approach, and the reader is referred to Ref. 91 and references therein for a more comprehensive overview. For electronic-structure codes employing a localized basis set, natural choices for Hubbard occupations are either Mulliken or Löwdin population matrices.⁹² In contrast, codes based on plane-wave basis sets often use atomic orbitals as projectors,^{8,93} whose localized functions are parameterized with free-atom calculations and then stored in the pseudopotentials. During the generation of pseudopotentials, the atomic orbitals are chosen to be orthonormal to all other orbitals centered on the same atom. However, this cannot guarantee orthogonality to orbitals localized on other sites during practical calculations. Hence, these projector functions are referred to as nonorthogonalized atomic orbitals (NAO).⁵⁴ While straightforward to implement and use, NAO may display spatially extended ‘tails’, potentially resulting in the same domain being tackled twice by Hubbard corrections if the atomic orbitals of two neighboring atoms overlap.

Truncation spheres⁹³ provide a means of ruling out such double counting by cutting off possible tails.¹ However, the radius of these spheres represents an additional parameter that affects the obtained occupation numbers.⁹⁴ The value of this parameter varies depending on the code utilized and may require manual adjustment (e.g., muffin-tin radius in the linearized augmented plane-wave approach) or can be embedded within the pseudopotential (typical

¹Note that this “double counting” must not be confused with the double counting term in DFT+ U energy functionals derived from the Hubbard model.

of projector-augmented-wave (PAW) pseudopotentials).

An alternative, parameter-free approach to circumvent truncation involves orthogonalizing NAO across all atomic sites, e.g., using Löwdin’s scheme,⁹⁵ thus transforming them into orthogonalized atomic orbitals (OAO).^{54,91} The resulting inter-site orthogonality clears the overlap of projectors on different sites⁹¹ and even accounts for possible hybridization between them, albeit to a limited extent. Several benchmark studies have shown that OAO projectors consistently outperform NAO projectors with respect to structural, electronic and spectral properties.^{45,54,69}

Finally, Wannier functions are also viable Hubbard projector functions.^{29,96,97} Specifically, maximally localized Wannier functions (MLWF)^{98,99} can separate manifolds in a system-specific fashion,¹⁰⁰ and can serve as effective Hubbard projector functions within the generalized DFT+ U framework presented in Eq. (6). Despite the extensive use of Wannier functions, their current adoption in DFT+ U calculations remains limited,^{55,101,102} possibly due to the non-trivial steps of finding an appropriate starting guess and disentangling overlapping bands during wannierization. Moreover, features relevant for practical studies such as the calculation of forces and stresses are cumbersome to implement.

2.3 LR-cDFT to compute orbital-resolved U parameters

LR-cDFT is based on using the DFT+ U energy functional to (heuristically) restore piecewise-linearity for the Hubbard manifold in (semi-)local DFT functionals suffering from electron self-interaction.^{8,12} An important manifestation of the latter are so-called fractional charge errors (FCE), which are spurious (usually convex) deviations from linearity of E_{DFT} with respect to fractional addition or removal of charge,¹⁵ i.e.,

$$\text{FCE} = \frac{\partial^2 E_{\text{DFT}}}{\partial q^2}, \tag{8}$$

where q represents the charge of the system under consideration. Inspection of Eq. (1) shows that the Hubbard U correction amounts to removing a quadratic term and adding a linear one, scaled by the numerical value of U . Note, however, that the curvature removed by Eq. (1) is not with respect to the total charge of the system q but instead with respect to the projected *local* occupation of the Hubbard manifold $\mathbf{n}^{I\sigma}$. Thus, a fundamental assumption is that the electrons in this localized Hubbard manifold are the most affected by self-interaction and can be dealt with separately. This interpretation makes it possible to define the value of Hubbard U as the one for which the second derivative of the total energy functional becomes zero with respect to changes in the occupation of the shell,⁸

$$U^I = \frac{\partial^2 E}{\partial(\Lambda^I)^2} \Big|_q, \quad (9)$$

where we now use $\Lambda^I = \sum_{\sigma} \sum_i^{2l+1} \lambda_i^{I\sigma}$ to define the local occupation of the Hubbard manifold. Because a direct control of orbital occupations is not tractable in codes that obtain them as output quantities, Lagrange multipliers α are introduced to linearly shift the potential of the Hubbard manifold and thus indirectly control Λ^I (see Refs. 7,8,27 for the derivation). Then, two response matrices are defined using finite differences:

$$(\chi)^{IJ} = \frac{\Delta\Lambda^I}{\Delta\alpha^J}, \quad (\chi_0)^{IJ} = \frac{\Delta\Lambda_0^I}{\Delta\alpha^J}, \quad (10)$$

where χ represents the self-consistent, screened response of the manifold, whereas χ_0 is due to the non-interacting, unscreened response coming from the re-hybridization of the atomic orbital projectors that results from the perturbation. In many plane-wave codes, these latter non-interacting orbital occupations Λ_0^I can be obtained from the first iteration in the self-consistent cycle of the perturbative calculation. Since the response χ_0 is unrelated to electron self-interaction, it must be subtracted from the interacting (i.e., screened) response when computing U :

$$U^I = (\chi_0^{-1} - \chi^{-1})^{II}. \quad (11)$$

In practice, the response functions are obtained by either applying multiple small (positive and negative) perturbations to the shells of interest of a converged ground state⁸ (with periodic systems requiring a supercell approach to avoid interactions between a perturbed Hubbard manifold and its periodic images) or from DFPT^{51,103} using the response to monochromatic perturbations in a primitive cell.

Orbital-resolved Hubbard U parameters can be evaluated using the formalism of Eqs. (10) and (11) by adapting the definition of the total occupation of the Hubbard manifold. In the most general case, every magnetic quantum orbital i of the nl subshell can acquire an individual Hubbard parameter. The occupation of such a manifold is given by

$$\Lambda_i^I = \sum_{\sigma} \lambda_i^{I\sigma}. \quad (12)$$

With this, the elements of the response matrices (Eq. (10)) can be redefined as

$$(\chi)_{ij}^{IJ} = \frac{\Delta\Lambda_i^I}{\Delta\alpha_j^J}, \quad (\chi_0)_{ij}^{IJ} = \frac{\Delta\Lambda_{i,0}^I}{\Delta\alpha_j^J}, \quad (13)$$

while the expression for the orbital-resolved on-site Hubbard U parameters becomes

$$U_{ij}^I = (\chi_0^{-1} - \chi^{-1})_{ij}^{II}. \quad (14)$$

The generalized formalism of Eq. (14) not only accommodates orbital-resolved on-site U parameters, but allows for the determination of inter-site parameters (U_{ij}^{IJ} with $I \neq J$, or, following the nomenclature of DFT+ U + V , V_{ij}^{IJ}), as well as on-site inter-orbital parameters (U_{ij}^{II} for $i \neq j$). Nevertheless, the primary emphasis of this study lies in investigating the on-site intra-manifold parameters $U_{ii}^{II} \equiv U_i^I$.

For the sake of illustration, let us consider a d shell of an atom exhibiting local O_h symmetry. Also, we assume that this atom be the only Hubbard atom in the system, thereby enabling us to neglect inter-site responses and to drop the superscript I . Then, one

can define an orbital-resolved Hubbard matrix of size 2×2 that reads

$$\begin{pmatrix} U_{t_{2g},t_{2g}} & U_{e_g,t_{2g}} \\ U_{t_{2g},e_g} & U_{e_g,e_g} \end{pmatrix} = \begin{pmatrix} (\chi_0)_{t_{2g},t_{2g}} & (\chi_0)_{e_g,t_{2g}} \\ (\chi_0)_{t_{2g},e_g} & (\chi_0)_{e_g,e_g} \end{pmatrix}^{-1} - \begin{pmatrix} (\chi)_{t_{2g},t_{2g}} & (\chi)_{e_g,t_{2g}} \\ (\chi)_{t_{2g},e_g} & (\chi)_{e_g,e_g} \end{pmatrix}^{-1}, \quad (15)$$

where the indices represent the response in occupations of manifold a to perturbation of manifold b , $(\chi)_{a,b} = \frac{\Delta\Lambda_a}{\Delta\alpha_b}$, for instance $(\chi)_{e_g,t_{2g}} = \frac{\Delta\Lambda_{e_g}}{\Delta\alpha_{t_{2g}}}$. [Pickett et al.](#) showed that the orbital-resolved matrix elements of Eq. (15) are related to the shell-averaged Hubbard parameter U through a sum rule.²⁷ A slightly adapted form of this rule that accounts for the role of the non-interacting response reads²

$$U = \left[\sum_{a,b=t_{2g},e_g} (\chi_0)_{a,b} \right]^{-1} - \left[\sum_{a,b=t_{2g},e_g} (\chi)_{a,b} \right]^{-1}. \quad (16)$$

The lesson to learn from Eq. (16) lies in the off-diagonal values of χ , whose physical implication consists in intra-shell screening (in this example $e_g \leftrightarrow t_{2g}$). Since the sign of these off-diagonal values is normally opposite to that of the diagonal ones³, they diminish the contribution of the term $\sum_{ab}(\chi)_{a,b}$, which may substantially increase U values upon computation of the inverse. Note that χ_0 is not affected by this, because the off-diagonal elements of the unscreened response are zero by definition (except for numerical noise). In the extreme scenario where perturbations are exclusively screened within the same shell, the sum over the off-diagonal elements equals the trace of χ , causing $\det(\chi)$ to approach zero, leading to $U \rightarrow \infty$. Consequently, if the current definition of the response matrices is used to compute orbital-resolved U parameters, the determinant required for the full inversion

²[Pickett et al.](#) define the d shell-averaged Hubbard parameter (in *their* notation) as $U_{dd} = \left[\sum_{a,b=t_{2g},e_g} (\chi)_{a,b} \right]^{-1}$, whereas in this work we use the definition of Eq. (16) due to the non-interacting (bare) response.

³This results from a physical necessity: if a perturbation to the potential of a manifold a causes the occupation of a to increase, the electrons must be borrowed from another manifold, whose orbital occupation will naturally decrease, since the global charge is kept constant in LR-cDFT.

of χ inadvertently reintroduces the shell-averaging of the response. This is evident in the findings of the aforementioned study by [Pickett et al.](#), where the computed $U_{t_{2g}}$ ($\equiv U_{t_{2g},t_{2g}}$) displayed only minimal differences compared to U_{e_g} ($\equiv U_{e_g,e_g}$) and the shell-averaged U .²⁷

In order to derive on-site U parameters that explicitly incorporate intra-shell screening effects, it is necessary to set the off-diagonal matrix elements of χ and χ_0 to zero before computing their inverses. This scheme was employed by [Linscott et al.](#), who refer to it as pointwise (“ 1×1 ”) inversion, in order to compute screened and spin-resolved Hubbard parameters for metal aquo complexes.⁵⁰ [Solovyev et al.](#) also applied this strategy, albeit implicitly, to obtain screened U parameters specific to t_{2g} in perovskites.⁷⁹ Although the removal of off-diagonal elements seems a drastic approximation, it allows for a more tailored definition of Hubbard manifolds compared to the conventional DFT+ U approach. The latter assumes (without proof) that ligand orbitals account for the majority of screening while the role of intra-shell interactions is neglected. In fact, several cRPA studies suggest that the opposite is true, showing that intra-shell screening can be as significant, or even more so, as inter-shell screening.^{86,87} An important caveat to the LR-cDFT approach that also affects the orbital-resolved form presented here is that unphysical U values may result when it is applied to fully occupied manifolds. This is a well-known limitation^{104,105} that follows from the fact that the response of a deep-lying state to a relatively small perturbation (≈ 0.05 eV) is often on the same order of magnitude as the numerical noise, leading to instabilities during the inversion of the response matrices.

3 Computational details

All calculations are carried out using the QUANTUM ESPRESSO distribution.^{106–108} We have incorporated the capability to utilize and determine orbital-resolved Hubbard U parameters with the `pw.x` code and will make this accessible in a future release. Structure and isosurface plots for pyrite (FeS_2) and pyrolusite ($\beta\text{-MnO}_2$) are generated using

VESTA.¹⁰⁹ Unless stated otherwise, all systems are structurally optimized using the Broyden-Fletcher-Goldfarb-Shanno (BFGS) algorithm¹¹⁰ with convergence thresholds of 10^{-4} Ry, 10^{-3} Ry/Bohr, and 0.5 kbar for the total energy, forces, and pressure, respectively. KS wavefunctions (charge density) are expanded in plane waves up to a kinetic-energy cutoff of 90 Ry (1080 Ry) using PBE¹¹¹ pseudopotentials for pyrite and the Fe(II) molecular complexes, and PBEsol pseudopotentials for β -MnO₂⁴ taken from the SSSP Precision library v. 1.1.1.2.^{115,116} The projected density of states (PDOS) is obtained using a Gaussian smearing with a broadening parameter of 0.02 Ry and employing the *diag-basis* feature of the `projwfc.x` code, which projects the wavefunctions onto the eigenstates of the occupation matrix rather than using unrotated atomic orbital projectors.⁵⁴ This allows for a clear distinction between t_g/t_{2g} and e_g states, regardless of the orientation of the global coordinate system. Fe(II) molecular complexes are simulated at a fixed +2 charge state in cubic boxes with an edge length of 15 Å and using only the Γ point to sample the Brillouin zone. The total magnetization of the molecular complexes is always fixed to either $4.0 \mu_B$ or $0.0 \mu_B$ in order to compute high-spin (HS) and low-spin (LS) configurations, respectively. The starting geometries of the Fe(II) molecular complexes are taken from the SI of Ref. 76, whereas experimental structures are chosen as a starting points for FeS₂ and β -MnO₂. The Brillouin zones of FeS₂ and β -MnO₂ are sampled with uniform Γ -centered Monkhorst-Pack meshes of sizes $9 \times 9 \times 9$ and $4 \times 4 \times 6$, respectively.

We use Löwdin-orthogonalized atomic orbitals as Hubbard projectors (OAO)^{91,95} for all DFT+ U calculations including those with orbital-resolved U parameters. Shell-averaged Hubbard parameters are evaluated using the DFPT implementation^{51,52} of the HP code (`hp.x`)⁶⁷ included in QUANTUM ESPRESSO, employing \mathbf{q} point meshes of size $2 \times 2 \times 2$ for FeS₂ and β -MnO₂, and $1 \times 1 \times 1$ for the Fe(II) molecular complexes, respectively. We compute orbital-resolved U parameters according to the LR-cDFT approach described in

⁴We used Fe.pbe-spn-kjpaw-ps1.0.2.1.UPF,¹¹² s_pbe_v1.4.uspp.F.UPF,¹¹³ 0.pbe-n-kjpaw-ps1.0.1.UPF,¹¹² H.pbe-rrkjus-ps1.1.0.0.UPF,¹¹⁴ P.pbe-n-rrkjus-ps1.1.0.0.UPF,¹¹⁴ C.pbe-n-kjpaw-ps1.1.0.0.UPF,¹¹⁴ N.pbe-n-radius_5.UPF (THEOS pseudo) and mn.pbesol_v1.5.uspp.F.UPF¹¹³ and 0.pbesol-n-kjpaw-ps1.0.1.UPF¹¹² for β -MnO₂.

Section 2 by applying perturbations of $\alpha = [-0.05, 0.05]$ eV to the manifold of interest and recording the non-interacting and interacting responses of the orbital occupations. To avoid interactions of perturbations with their periodic images, the calculations of FeS₂ and β -MnO₂ are conducted in a $2 \times 2 \times 2$ supercell containing 96 atoms. We emphasize that DFPT and LR-cDFT are equivalent by construction, and therefore yield the same Hubbard parameters when applied to identical systems.⁵¹ As the orbital response depends on the system’s electronic structure, calculated Hubbard parameters may vary significantly when transitioning from a PBE/PBEsol ground state to a PBE/PBEsol+ U one. Therefore, to achieve self-consistency of the computed U values, we employ an iterative procedure that consists of structural optimizations and subsequent perturbative calculations.^{30,52,117} This procedure is repeated until the difference between the input and output parameters falls below the predefined threshold of ~ 0.1 eV. The resulting Hubbard parameters are reported in Section 4.

4 Results and discussion

4.1 Pyrite (FeS₂)

4.1.1 Challenging theoretical description

Under normal conditions, pyrite is the stable polymorph of FeS₂ and crystallizes in the cubic space group Pa $\bar{3}$ with an experimental lattice parameter $a = 5.418$ Å.¹¹⁸ The crystal structure, shown in Figure 1, consists of S₂ dimers octahedrally coordinating Fe²⁺ ions, which form a *fcc* sublattice.¹¹⁹ At 0 K, the compound is diamagnetic ($S = 0$) due to the preferred LS configuration of the Fe²⁺ ions. Pyrite’s natural abundance, optical band gap of ~ 0.95 eV, and large optical absorption coefficient make it an appealing material for photovoltaic applications. Nevertheless, despite theoretical predictions suggesting an open circuit voltage of ~ 0.71 V based on the Shockley-Queisser equations, experimental results have consistently

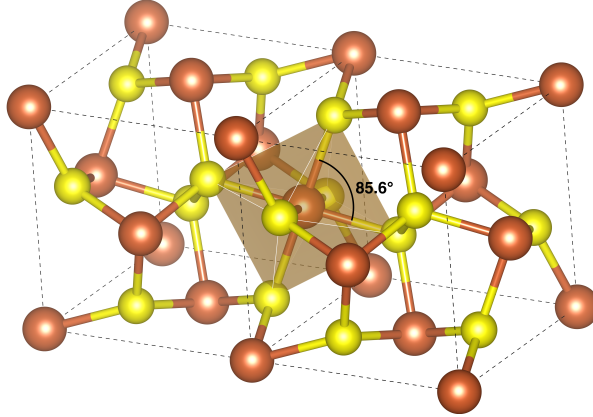


Figure 1: The experimental crystal structure of pyrite (FeS_2). Fe (brown) is octahedrally coordinated by S (yellow), which also forms characteristic S–S dimers. The octahedra are slightly distorted and display angles different from 90° .

fallen short, typically measuring values around 0.2 V.¹²⁰ This discrepancy is among several reasons motivating an accurate quantum-mechanical description of pyrite’s ground state.

In early DFT studies, the LDA functional demonstrated exceptional accuracy in predicting the equilibrium volume, band gap, and relative energy levels of the S-3*p* bands compared to the valence band maximum (VBM).^{119,121} PBE¹¹¹ and AM05¹²² provide a qualitatively similar picture but underestimate the band gap by about 0.5 eV and 0.75 eV, respectively.¹²⁰

At first glance, the dominant e_g contributions in the conduction band (Figure 2) indicate Mott-Hubbard insulation. However, a more detailed analysis of the electronic band structure (Figure 3) reveals that the conduction band minimum (CBM), located at the Γ point, is composed of a d - p σ^* hybrid orbital with dominant S-3*p_z* contributions. This observation holds the key to understanding why numerous electronic structure methods, including more advanced approaches, face challenges in improving the prediction of the band gap beyond the capabilities of PBE. For instance, when employing G_0W_0 , the small PBE band gap diminishes further.¹²⁴ In contrast, hybrid functionals such as PBE0,¹²⁵ HSE06,¹²⁶ DSH,¹²⁷ and M06¹²⁸ overestimate its value by more than 1 eV.¹²⁹ Previous PBE+ U studies focused on correcting the Fe- d shell using shell-averaged Hubbard parameters. For example, Sun et al.

⁵The point group symmetry of Fe in pyrite is T_h , rather than O_h ; thus, the triply degenerate irreducible representation is correctly named t_g instead of t_{2g} .¹²³

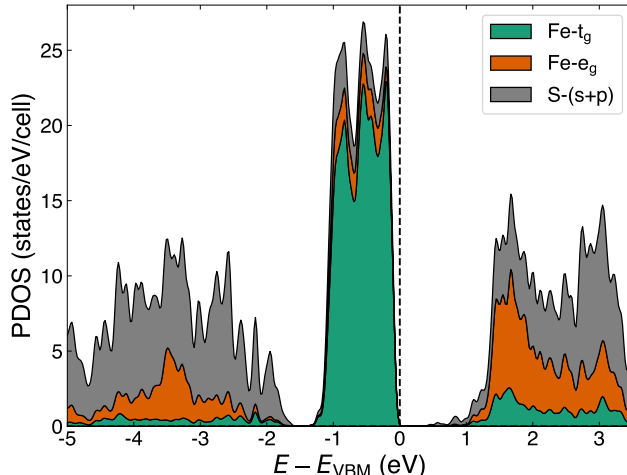


Figure 2: Stacked projected density of states (PDOS) of the nonmagnetic PBE ground-state of pyrite FeS_2 . The small t_g contributions⁵ in the conduction band and the e_g contributions close to the VBM are likely projection artifacts resulting from the slightly canted geometry of the FeS_6 octahedra.

applied $U = 2.0 \text{ eV}$ (with PAW projectors),¹²⁰ whereas Schena *et al.* used a combination of $U = 3.0 \text{ eV}$ with $J = 1.0 \text{ eV}$ (Muffin-Tin sphere projectors).¹²⁴ Notably, no set of *ab initio* computed Hubbard parameters has been published for this material to date, to the best of our knowledge. The rationale behind the use of empirical parameters likely lies in a pronounced influence of shell-averaged U corrections on the equilibrium properties, as we demonstrate hereinafter.

4.1.2 Double impact of shell-averaged U corrections

We perform PBE+ U calculations incorporating empirical on-site Hubbard U corrections ranging from 1.0 to 5.0 eV and analyze their impact on the estimated band gap and on the crystal structure. To differentiate between a band gap broadening caused by structural changes and one resulting directly from the influence of U on the electronic structure, we perform the calculations under three different constrained conditions. Initially, we retain the PBE ionic structure, keeping the cell vectors and ionic positions fixed (setup 1). Subsequently, we perform another set of calculations with ionic position relaxations while maintaining a constant cell volume (setup 2). Lastly, we conduct full optimization, allow-

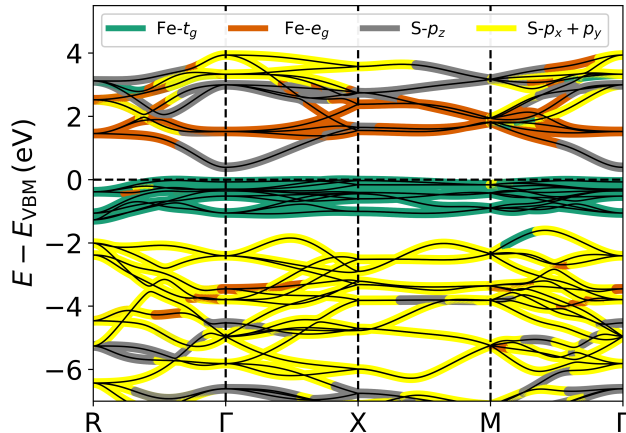


Figure 3: (Fat-)Band structure of pyrite computed using the PBE functional. The coloring indicates the most dominant contribution of the manifolds to the individual bands. The uppermost valence bands are predominantly Fe- t_g , whereas the conduction bands display a strong S- $3p_z$ character at Γ but Fe- e_g character elsewhere. Thus, the band gap of pyrite is not a $d-d$ transition, but a $d-p$ one.

ing for simultaneous adjustments of both ionic positions and cell vectors (setup 3). While band gaps are fundamentally outside the realm of DFT, DFT+ U should improve upon the performance of the uncorrected functional as long as the compound’s frontier states are well-represented by the Hubbard manifold.^{45,57} For this case, one can argue that the Hubbard U corrections (locally) act in the spirit of a Koopmans-compliant functional.¹⁷

Figure 4 illustrates that even when no ionic relaxation is considered (setup 1), the band gap slowly but steadily expands with increasing U values. The shifts in band eigenvalues indicate that this expansion primarily stems from a downshift of the t_g orbitals’ KS potential in the valence region (see Table SI 1). On the other hand, the CBM remains largely unaffected by the Hubbard correction with the corresponding eigenvalues showing minimal changes. Consistent with previous studies, we find that the experimental band gap is accurately reproduced at $U \approx 2.0$ eV, but is overestimated by approximately 53% at $U = 5.0$ eV. This overestimation of the band gap at such moderate values of U is surprising since the CBM, consisting of S- $3p_z$ states, is not included in the Hubbard manifold, and its local deviation from PWL remains uncorrected. Upon relaxing the ionic positions while keeping the cell volume constant (setup 2), the band gap shows a more sensitive response to higher values

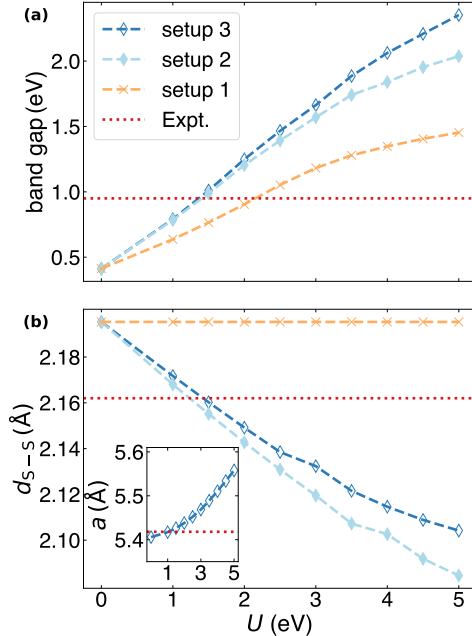


Figure 4: **(a)** calculated band gaps and **(b)** S–S bond lengths computed with PBE+ U using three setups: at fixed cell and ionic positions (setup 1); at constant cell volume relaxing the ionic positions (setup 2); and relaxing both the ionic positions and the cell volume (setup 3). The inset in the bottom panel shows the dependence of the lattice parameter on U during volume relaxations. Red dashed horizontal lines correspond to the experimental values.^{118,130}

of U . The experimental band gap is already achieved at $U \approx 1.5$ eV and is overestimated by 115% at $U = 5.0$ eV. This trend becomes even more pronounced when relaxation of the cell vectors is enabled (setup 3), resulting in a band gap overestimation of 147% at $U = 5.0$ eV. As shown in Figure 4(b), the additional expansion following ionic relaxations is correlated with a significant contraction of the S–S bonds. This aligns well with the findings of Eyert et al., who pointed out that the S–S bond length governs the band gap, as it controls the dispersion of the lowest conduction band around the Γ point.¹²¹ Remarkably, in variable-cell calculations (setup 3) the S–S bonds continue to contract with increasing values of U , despite the simultaneous growth of the lattice parameter (inset of Figure 4(b)). The differences observed between relaxed and fixed structure calculations reveal that shell-averaged U corrections modify the band gap through two distinct mechanisms: first, through the expected downshift of the valence band eigenvalues, and second by causing pronounced contractions of the S–S bonds.

We now shift our focus from conventional equilibrium properties to investigate the underlying reasons behind the substantial influence of shell-averaged U corrections on these bonds, which can be elucidated by examining the occupations of the individual orbitals. Table 1 presents the eigenvalues of the Fe- d occupation matrix and the corresponding Hubbard energies E_U for an illustrative case with $U = 3.0$ eV, both prior to and after complete structural relaxation. As the eigenvalues of the t_g orbitals (d_{xy} , d_{xz} , d_{yz}) approach idempotency, this manifold is responsible for the smaller share of the overall Hubbard energy, approximately 33%. In contrast, the e_g orbitals ($d_{x^2-y^2}$ and d_{z^2}) contribute to nearly 66% of the total Hubbard energy due to possessing occupation eigenvalues far from either 0 or 1. Structural relaxation induces both intra-shell and inter-shell charge transfers that allow for a 6% reduction of the total Hubbard energy. At the intra-shell level, the occupation of t_g orbitals grows at the expense of e_g . Even more significantly, the overall d -occupancy slightly drops from 6.996 to 6.970, indicating a migration of some e_g electrons into adjacent S- p orbitals. This transfer of charge effectively enhances the S-S bond order and leads to the observed contraction of d_{S-S} . Thus, the unexpectedly potent influence of the value of U on the band gap is rooted in the correction of the e_g manifold.

Table 1: Occupation eigenvalues λ and corresponding Hubbard energies E_U obtained for the Fe- d orbitals in FeS₂ using PBE+ U with $U = 3.0$ eV. Results are shown for the fixed PBE structure (setup 1, $a = 5.406$ Å and a S-S distance of 2.195 Å, top) and after structural relaxation (setup 3, $a = 5.469$ Å and a S-S distance of 2.132 Å, bottom). The last column shows the total occupations ($2 \sum \lambda$) and Hubbard energies ($2 \sum E_U$), which correspond to twice the sum (due to spin degeneracy) of the individual contributions.

	Orbital	$d_{x^2-y^2}$	d_{z^2}	d_{xy}	d_{xz}	d_{yz}	2Σ
setup 1	λ	0.383	0.383	0.901	0.901	0.930	6.996
	E_U (meV)	354	354	134	134	98	2148
setup 3	λ	0.359	0.359	0.915	0.915	0.937	6.970
	E_U (meV)	343	343	117	117	89	2018

We recall that the eigenvalues listed in Table 1 are not universal quantities but the result

of a projection of the KS wave functions onto atom-centered OAO. The accuracy of on-site occupations provided by atomic-like projectors relies on the similarity between a given orbital’s shape in the system under inspection and that in a free atom, since the general shape and extension of projector AOs is typically determined in free atom calculations. However, one-center projections using atomic orbitals struggle to account for strong orbital hybridization, where electrons localize ‘off-site’ between the bonded atoms. In the case of FeS₂, the t_g manifold is only marginally bonding, while the formally unoccupied e_g orbitals form σ MOs with neighboring S-3 p_z orbitals. Consequently, it is misleading to interpret the eigenvalues corresponding to $d_{x^2-y^2}$ and d_{z^2} as indicative of actual on-site orbital occupancies in the context of Hubbard U corrections. Moreover, their numerical values significantly hinge on computational factors like the chosen pseudopotentials and the specific charge state for which they were parameterized.^{56,121}

Within the setup of this study, the U correction effectively penalizes the hybridization between Fe and S; however, the use of different Hubbard projector functions cause the opposite effect, for example, if NAO projectors yield e_g eigenvalues larger than 0.5. In this case, the Hubbard correction would draw electrons into the e_g manifold rather than expelling them (see Eq. (3)).

4.1.3 Absence of intra-shell screening in shell-averaged LR-cDFT

Having investigated how the shell-averaged U parameter affects equilibrium observables, our focus now shifts to understanding the implications when this parameter is determined from first principles. Applying DFPT to the PBE ground state of FeS₂ yields a U value of 7.37 eV. After undergoing four iterations within the self-consistency loop detailed in Section 2.3, U converges to 6.47 eV. Unfortunately, neither of these parameters can reasonably reproduce the experimental characteristics of pyrite. In fact, both values result in the stabilization of a spurious ferromagnetic ground state ($2\mu_B/\text{cell}$) in unrestricted open-shell calculations. For comparison, all of the following U parameters and observables are reported for the

nonmagnetic ground state that was enforced by fixing the total magnetization to $0.0 \mu_B$.

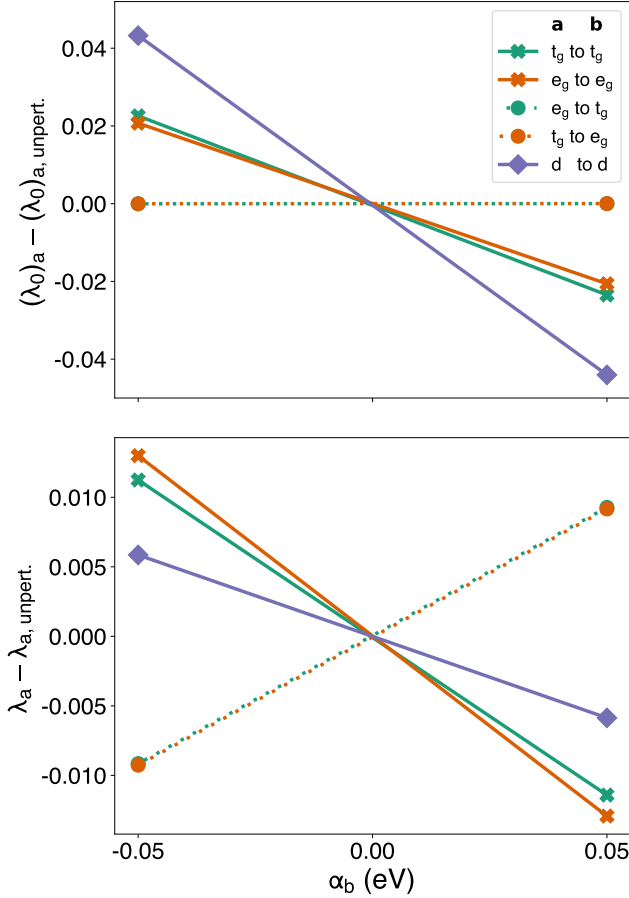


Figure 5: Unscreened/non-interacting (top) and screened/interacting (bottom) responses of the occupations λ of manifolds “a” to perturbations α applied to manifolds “b” in FeS₂, obtained through the orbital-resolved LR-cDFT approach. The starting point is the fully relaxed PBE ground state.

The reason for this significant overestimation of the shell-averaged Hubbard U parameter can be understood from Figure 5, which shows the response of orbital occupancies to perturbations for both the entire $3d$ -shell and for its irreducible representations t_g and e_g . This information cannot be extracted from shell-averaged LR-cDFT, but can be recovered by adopting the orbital-resolved approach. The substantial opposing responses of e_g occupations to perturbations of t_g and vice versa (depicted by dashed lines in the bottom panel) suggest the presence of a robust intra-shell $t_g \leftrightarrow e_g$ screening channel. Inserting the values

of χ_0 and χ (represented by the line slopes in Figure 5) into Eq. (16), one obtains

$$\begin{aligned}
 U &= \left[\sum \begin{pmatrix} -0.4608 & 0.0001 \\ 0.0001 & -0.4131 \end{pmatrix} \right]^{-1} - \left[\sum \begin{pmatrix} -0.2266 & 0.1843 \\ 0.1843 & -0.2592 \end{pmatrix} \right]^{-1} \\
 &= (-0.8737)^{-1} - (-0.1172)^{-1} = -1.144 - (-8.532) = 7.388 \text{ eV}, \quad (17)
 \end{aligned}$$

where the first and second matrix represent the unscreened and the screened responses, respectively. Note the almost perfect agreement between this LR-cDFT Hubbard parameter ($U = 7.39 \text{ eV}$) and the one derived from DFPT ($U = 7.37 \text{ eV}$); the minor discrepancies are due to numerical noise. The individual matrix elements of Eq. (17) reveal that the apparent overestimation of the shell-averaged Hubbard parameter primarily stems from the suppression of intra-shell screening that occurs due to the simultaneous perturbation of the t_g and the e_g manifolds. While the individual screened responses of the t_g and e_g orbitals are substantial ($\chi_{t_g, t_g} = -0.2266 \text{ eV}^{-1}$ and $\chi_{e_g, e_g} = -0.2592 \text{ eV}^{-1}$), the overall response of the d shell is massively reduced by the off-diagonal elements of χ (both 0.1843 eV^{-1}). Inversion of this *apparently* small screened response of the d shell (-0.1172 eV^{-1}) yields $\chi^{-1} = -8.532 \text{ eV}$, which is what ultimately fuels the overestimation of the shell-averaged Hubbard parameter.

It should be noted that this shell-averaged U parameter also encompasses, to a certain extent, the response of the S-3 p orbitals, because the e_g eigenstates likely contain substantial S-3 p contributions. With these insights in mind, it becomes pertinent to investigate whether the orbital-resolved approach to Hubbard U can offer improvements over the unsatisfactory performance of shell-averaged PBE+ U .

4.1.4 Application of the orbital-resolved U

Employing the orbital-resolved LR-cDFT methodology detailed in Section 2.3, we proceed to compute individual Hubbard parameters for the t_g and e_g orbitals of FeS₂. Prior to inverting

the response matrix, all off-diagonal intra-shell matrix elements are set to zero:

$$(\chi)_{i \neq j}^{II} = 0, \text{ and } (\chi_0)_{i \neq j}^{II} = 0. \quad (18)$$

This ensures that the resulting orbital-resolved Hubbard parameters incorporate the effect of $t_g \leftrightarrow e_g$ screening. The parameters U_{t_g} and U_{e_g} converge rapidly, reaching their self-consistent values of 3.29 eV and 2.16 eV, respectively, within just three iterations of self-consistency.

The final response matrices read

$$\begin{aligned} \begin{pmatrix} U_{t_g} & 0 \\ 0 & U_{e_g} \end{pmatrix} &= \left[\begin{pmatrix} -0.3516 & 0 \\ 0 & -0.1948 \end{pmatrix} \right]^{-1} - \left[\begin{pmatrix} -0.1998 & 0 \\ 0 & -0.1187 \end{pmatrix} \right]^{-1} \\ &= \begin{pmatrix} 3.29 & 0 \\ 0 & 2.16 \end{pmatrix}. \end{aligned} \quad (19)$$

Following the approach of [Solovyev et al.](#), one may also exclusively target the t_g manifold and not correct the e_g states at all. This choice is driven by the expectation that interactions of genuine *on-site* character should manifest within the occupied t_g orbitals rather than in the hybridized and formally empty e_g manifold. Moreover, as previously stated, it is unlikely that one-center atomic orbital projectors are suited to provide meaningful on-site occupation numbers for the e_g orbitals. With U_{e_g} corrections absent, the converged value of U_{t_g} slightly decreases to 3.01 eV. Having established the necessary parameters, we now focus on their impact in practical calculations. [Table 2](#) shows that the orbital-resolved approach consistently outperforms the shell-averaged approach, except when U is tuned empirically (U^{emp}). When utilizing only U_{t_g} , both the lattice parameter and the S–S bond length exhibit deviations of less than 1% from the experimental values. With orbital-resolved corrections applied to t_g and e_g , this agreement with the experimental data is slightly worsened but

Table 2: Comparison of the equilibrium lattice parameter a , the S–S bond length $d_{\text{S-S}}$ and the band gap E_g of pyrite derived from Hubbard-corrected PBE calculations targeting different manifolds. On-site Hubbard U_1 and U_2 refer to various parametrizations of the PBE+ U approach, while V is the inter-site Hubbard parameter of the PBE+ U + V approach.

	PBE	+ U	+ U + V	+ U^{emp}	+ U_{t_g} + U_{e_g}	+ U_{t_g}	Expt.
U_1 (eV)	—	6.47	6.73	1.50	3.29	3.01	—
U_2 or V (eV)	—	—	0.62	—	2.16	—	—
a (Å)	5.41	5.63	5.51	5.43	5.46	5.44	5.42 ¹¹⁸
$d_{\text{S-S}}$ (Å)	2.20	2.10	2.12	2.16	2.13	2.14	2.16 ¹¹⁸
E_g (eV)	0.41	2.63	2.06	1.00	1.70	1.45	0.95 ¹³⁰

still surpasses that of shell-averaged PBE+ U , where the lattice parameter deviates by 4%. Furthermore, the significant overestimation of the band gap amounting to 177% in the case of shell-averaged PBE+ U is substantially mitigated to 53% when switching to U_{t_g} . The DFT+ U + V approach yields noticeable improvements compared to the traditional + U approach; however, it appears that the inter-site V term lacks the strength to fully restore the hybridization between Fe and S that is suppressed by the shell-averaged on-site term. Therefore, the estimation of the lattice parameters and the band gap still remains notably worse than for the orbital-resolved PBE+ U approach.

These results underscore the critical importance of the choice of the Hubbard manifold in DFT+ U calculations for the FeS₂ polymorph pyrite. Under the shell-averaged approximation, the ground-state properties are extremely sensitive to the numerical value of U . This sensitivity primarily arises due to the correction of the hybridized e_g part of the d shell. Moreover, the shell-averaged Hubbard parameter derived from LR-cDFT lacks full screening, as the intra-shell screening channel ($t_g \leftrightarrow e_g$) is deactivated during the concurrent perturbation of both manifolds. On the other hand, the orbital-resolved approach accounts for intra-shell screening during perturbative calculations, resulting in significantly smaller Hubbard parameters. We have shown that correcting the localized Fe- t_g manifold alone suffices to obtain structural properties in very good agreement with experimental data, all without requiring

empirical adjustments to the parameters. A viable option for further improvements involves supplementing the orbital-resolved U corrections with inter-site V terms, as discussed in Section 5. Additionally, the PWL condition should also be enforced for the S- $3p_z$ orbital composing the CBM. Given the strong sp^3 hybridization of S, this would, however, require an adaption of the atomic-like projectors used in this study.

4.2 Fe(II) molecular complexes

4.2.1 Adiabatic spin energy differences

A crucial quantity for many TM compounds is the total energy difference between their HS and LS states, denoted as:

$$\Delta E_{H-L} = E_{tot}^{HS} - E_{tot}^{LS} . \quad (20)$$

Based on calculations of six Fe(II)-hexacomplexes, [Mariano et al.](#) showed that shell-averaged Hubbard U corrections to PBE and LDA introduce an unphysical bias against LS configurations, primarily due to substantial discrepancies in the Hubbard energies of LS and HS complexes.⁷⁶ This arises from the electron occupation patterns: LS-Fe(II) complexes exhibit a t_{2g}^6/e_g^0 electron configuration, while HS complexes a t_{2g}^4/e_g^2 configuration. In octahedral coordination environments, *unoccupied* e_g orbitals display substantial σ overlap with neighboring ligand orbitals. Consequently, in LS-Fe(II) all four e_g spin-orbitals can adopt fractional occupation eigenvalues, whereas in HS-Fe(II) this only applies to two spin-orbitals, as the other two are fully occupied. Considering that the Hubbard energy functional (Eq. (1)) induces corrections of up to $U/2$ eV for fractional occupations, but of 0 eV for idempotent occupations, Hubbard energies of LS-Fe(II) tend to be larger than those of HS-Fe(II). Furthermore, the LR-cDFT approach was shown to generate larger shell-averaged U parameters for LS-Fe(II) compared to HS-Fe(II),⁷⁶ thus enhancing this disparity.

In the following, we investigate whether the orbital-resolved DFT+ U approach can rectify the unphysical bias against LS states and deliver accurate adiabatic spin energy dif-

Table 3: PBE+ U manifolds and their calculated on-site parameters in eV. For t_{2g} the same parameter was applied to LS and HS complexes. The complexes are sorted in ascending order according to the ligand’s field strength.

Complex	manifold I	manifold II	$U_{t_{2g}}^{\text{LS}}$	U^{LS}	$U_{e_g}^{\text{HS}}$	U^{LS}	U^{HS}
$[\text{Fe}(\text{H}_2\text{O})_6]^{2+}$	e_g	—	—	4.28	2.69	5.71	4.13
$[\text{Fe}(\text{NH}_3)_6]^{2+}$	e_g	—	—	3.64	3.07	6.14	4.43
$[\text{Fe}(\text{NCH})_6]^{2+}$	t_{2g}	$t_{2g}+e_g$	7.05	2.12	1.87	6.76	5.53
$[\text{Fe}(\text{PH}_3)_6]^{2+}$	t_{2g}	$t_{2g}+e_g$	4.13	2.29	2.12	6.88	4.78
$[\text{Fe}(\text{CO})_6]^{2+}$	t_{2g}	$t_{2g}+e_g$	4.63	1.92	1.89	7.16	5.43
$[\text{Fe}(\text{CNH})_6]^{2+}$	t_{2g}	$t_{2g}+e_g$	4.64	2.13	1.72	7.43	5.79

ferences. For this purpose, we compute ΔE_{H-L} for all six octahedrally coordinated Fe(II)-hexacomplexes studied in Ref. 76 and benchmark the results against coupled-cluster corrected CASPT2 (CASPT2/CC)¹³¹ values, which are also taken from Ref. 76. We compare the performance of two distinct Hubbard manifolds. In **manifold I**, Hubbard corrections are applied either only to e_g states ($[\text{Fe}(\text{H}_2\text{O})_6]^{2+}$ and $[\text{Fe}(\text{NH}_3)_6]^{2+}$) or to only t_{2g} states ($[\text{Fe}(\text{NCH})_6]^{2+}$, $[\text{Fe}(\text{PH}_3)_6]^{2+}$, $[\text{Fe}(\text{CO})_6]^{2+}$, $[\text{Fe}(\text{CNH})_6]^{2+}$). While it would be desirable to obtain t_{2g} -specific Hubbard parameters for the former two compounds, this proves elusive due to the fact that the t_{2g} orbitals are fully occupied in the numerical sense ($\lambda \geq 0.997$) and thus respond non-linearly to perturbations.¹⁰⁴ For the same reason, no $U_{t_{2g}}^{\text{HS}}$ parameters could be computed for the HS complexes either. Therefore, all Hubbard corrections to t_{2g} states utilize the $U_{t_{2g}}^{\text{LS}}$ value. In **manifold II**, both t_{2g} and e_g orbitals are corrected simultaneously. When comparing the present work with Ref. 76, it is important to note that we use OAO projector functions and self-consistent procedures for geometry relaxations and determination of Hubbard terms. A comprehensive list of all complexes, the Hubbard manifolds considered and the corresponding orbital-resolved and shell-averaged U parameters is provided in Table 3.

The resulting adiabatic spin energy differences are visualized in Figure 6. Additionally, Table 4 lists the mean absolute error (MAE) of the different corrections against the

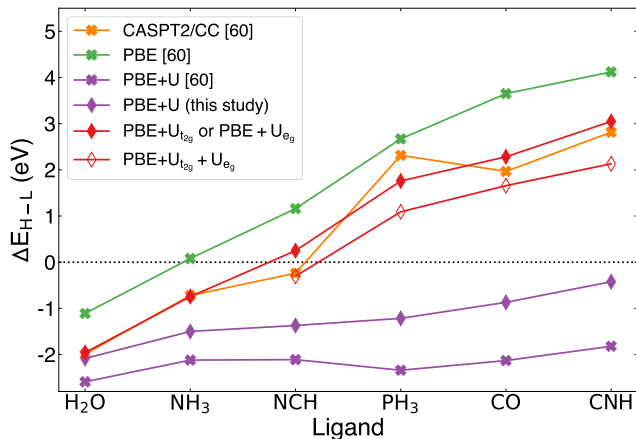


Figure 6: Adiabatic spin energies calculated for six Fe(II)-hexacomplexes using different DFT corrections and CASPT2/CC as the reference method. Data for PBE, PBE+ U , and CASPT2/CC was taken from the SI of Ref. 76.

CASPT2/CC¹³¹ reference values. In line with the findings of [Mariano et al.](#), shell-averaged PBE+ U drastically overstabilizes HS configurations and fails to reproduce the trend of increasing ΔE_{H-L} . Conversely, uncorrected PBE displays its known bias towards LS configurations. The introduction of orbital-resolved U corrections substantially enhances the predictive accuracy across all complexes analyzed, outperforming both PBE and the shell-averaged PBE+ U by a large margin. Correcting either t_{2g} or e_g (manifold I) closely aligns adiabatic spin energy differences with the CASPT2/CC values, resulting in the lowest MAE of 0.27 eV. The simultaneous correction of t_{2g} and e_g (manifold II) yields a slightly higher MAE of 0.57 eV, with larger deviation particularly for $[\text{Fe}(\text{PH}_3)_6]^{2+}$ and $[\text{Fe}(\text{CNH})_6]^{2+}$, but a better agreement for $[\text{Fe}(\text{NCH})_6]^{2+}$. In general, U_{e_g} corrections are smaller and less significant for the overall quantitative agreement than $U_{t_{2g}}$ corrections, since the t_{2g} orbitals host more – and more localized – electrons. The good overall agreement (qualitative *and* quantitative) of orbital-resolved PBE+ U with the CASPT2/CC data is surprising since the latter is a multiconfigurational approach, while the former can only improve the accuracy of a single reference state.

The good performance of the orbital-resolved U compared to the shell-averaged approach stems from two main factors. First, excluding the e_g orbitals from the Hubbard manifold of

Table 4: Mean absolute error (MAE) of ΔE_{H-L} for various Hubbard correction manifolds against the CASPT2/CC reference value from Ref. 76.

	PBE ⁷⁶	+ U	+ $U_{t_{2g}}$ or + U_{e_g}	+ $U_{t_{2g}}$ + U_{e_g}
MAE (eV)	1.07	1.94	0.27	0.57

strong-field complexes (manifold I) eliminates the primary cause of spuriously large Hubbard energies. Again, the exclusion of e_g orbitals can be justified with the inadequate representation of their strongly hybridized character by atomic orbital projectors. Second, even when the e_g orbitals are included (manifold II), independently computed U_{e_g} parameters are significantly smaller than $U_{t_{2g}}$ or shell-averaged U parameters owing to the explicit incorporation of intra-shell screening. For instance, in $[\text{Fe}(\text{CO})_6]^{2+}$ $U_{e_g}^{\text{LS}} = 1.92$ eV compared to $U^{\text{LS}} = 7.16$ eV. Hence, the orbital-resolved approach effectively diminishes the impact of non-ideal Hubbard projectors.

4.2.2 Piece-wise linearity of the total energy

As mentioned earlier, the use of on-site Hubbard U corrections in (semi-)local DFT is motivated by the mitigation of SIE, which have been linked to the spurious global deviation from PWL of the total energy with respect to fractional addition or removal of electronic charge q to the entire system.^{12,15,132} However, a study by Zhao et al. indicates that (shell-averaged) U corrections to TM d shells might be unfit for this purpose for a wide range of TM/ligand combinations when the Hubbard U parameters are derived from LR-cDFT.¹⁵

Thus, to directly benchmark the performance of orbital-resolved DFT+ U , we explicitly determine the global curvature following the approach presented in Ref. 15. For our analysis, we chose the strongest ligand complex $[\text{Fe}(\text{CNH})_6]^{q+}$ and perform several fixed-charge calculations where the total charge is varied between $q = 2$ and $q = 3$ in increments of $0.1e^-$. A useful metric to assess a functional’s deviation from PWL is given by E_{dev} , which is computed by subtracting the DFT total energy of a fractional charge calculation from the linear interpolation between the energies of the integer-charge endpoints $E_{\text{tot}}(q = 2)$ and

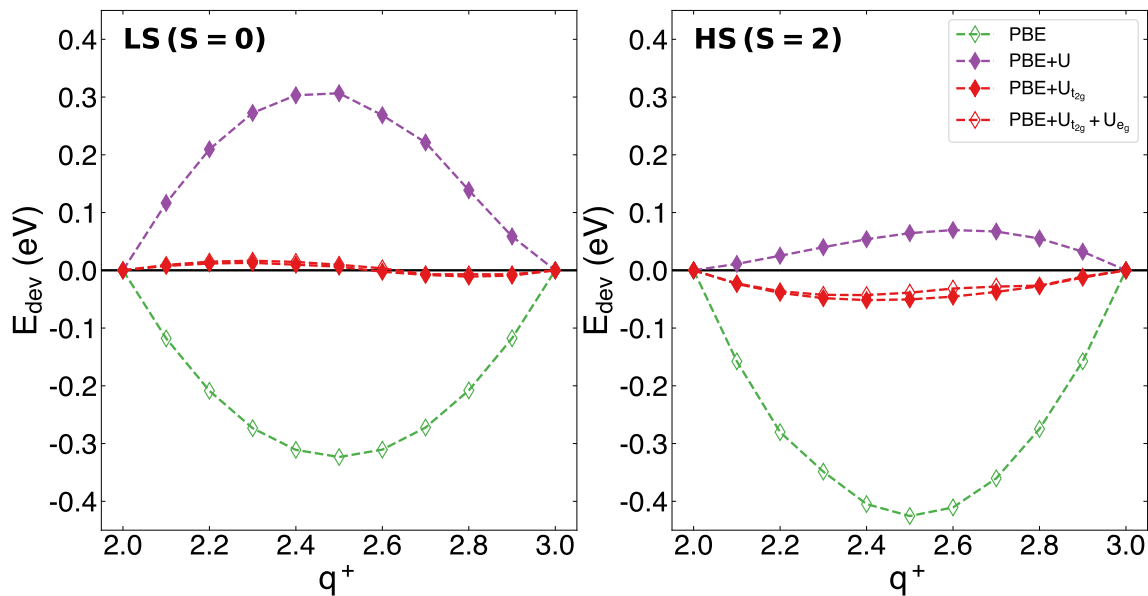


Figure 7: Deviation from piecewise linearity of the total energy upon fractional addition/removal of charge of $[\text{Fe}(\text{CNH})_6]^{(q+)}$ in low-spin (left) and high-spin (right) configurations. Note that the data points of $\text{PBE}+U_{t_{2g}}$ and $\text{PBE}+U_{t_{2g}} + U_{e_g}$ overlap in the LS case.

$E_{tot}(q = 3)$. Note that this explicit approach differs from the method employed by [Mariano et al.](#), who approximate E_{dev} using a cubic interpolation parameterized by the energy difference $\Delta E_q = E_{tot}(q = 2) - E_{tot}(q = 3)$ and the HOMO and LUMO eigenvalues of the integer-charge system.⁷⁶

Figure 7 shows that while shell-averaged Hubbard U corrections markedly reduce the deviation from PWL of HS $[\text{Fe}(\text{CNH})_6]^{q+}$, the global curvature of the LS compound is not eased. In fact, in the LS case the typical convex-shaped FCE displayed by bare PBE is transformed into a concave one of similar magnitude. In contrast, the orbital-resolved corrections reduce the deviation from PWL by an order of magnitude for both the LS and the HS configurations. It is worth noting that the remaining curvature barely differs between manifold I ($+U_{t_{2g}}$ only) and manifold II ($+U_{t_{2g}} + U_{e_g}$). Again, this observation is likely related to the low numerical value of the U_{e_g} parameters, which further supports the previous assumption that the primary contributor to the FCE is the rather localized t_{2g} manifold. For the same reason, applying U corrections to ligand orbitals like C- p is unlikely to significantly affect the FCE.

4.3 The importance of correcting ligand states in β -MnO₂

Unlike in TM sulfides, partially filled d shells of TM oxides are a frequent target for on-site corrections (see the discussion e.g. in Ref. 73). While Mott-Hubbard insulators such as the prototypical wüstite (FeO) present an energy gap separating different d states, so-called charge-transfer insulators, often involving highly oxidized and/or heavy TM species, exhibit O- $2p \rightarrow d$ band gaps.¹³³ The significant fraction of electrons localized on O- $2p$ orbitals adds complexity to the definition of the Hubbard manifold for DFT+ U calculations, as studied below for the case of β -MnO₂.

Crystallizing in the rutile structure (space group $P4_2/mnm$), β -MnO₂ displays a complex helical (screw-type spiral) antiferromagnetic (AFM) ordering below $T_N = 92$ K.¹³⁴ As done here, this ordering can be approximated by a collinear arrangement of the Mn⁴⁺ ions along [001], referred to as A1-AFM.⁶⁹ Considerable uncertainty surrounds the electronic properties of β -MnO₂. Sato et al. measured a large electrical resistivity at 0.3 K, suggesting insulating behavior.¹³⁴ However, the magnitude of the band gap has not been yet determined with universally accepted accuracy. Mid-twentieth-century works reported narrow band gaps around 0.26 – 0.28 eV,^{135,136} while more recent optical absorption studies reported much larger values ranging from 1.5 eV (nanocacti and nanorods)¹³⁷ to 2.0 eV for β -MnO₂ nanostructures grown on fluorine-doped tin oxide.¹³⁸ These results align with a reported hybrid functional DFT (PBE0) value of 1.5 eV, but not with a prediction of the closely related HSE03 functional (0.6 eV).¹³⁹ Previous works employing the shell-averaged DFT+ U approach suggest that a band gap is not opened unless the Mn- d states are corrected using U values larger than 6 eV.^{54,139} In general, the calculated properties are sensitive to the choice of projector functions. For instance, NAO projectors stabilize a ferromagnetic ordering, whereas OAO projectors favor the expected A1-AFM ordering.⁵⁴ Only by adding inter-site V between Mn- d and O- p states⁵⁴ or Hund's J corrections,¹⁴⁰ small gaps ranging from 0.25 to 0.32 eV emerge. A band gap of 0.8 eV was also obtained⁸³ with the anisotropic DFT+ U + J approach of Czyżyk and Sawatzky. In this method, shell-averaged Hubbard U and J corrections are

augmented with orbital-resolved $U_{mm'}$ and $J_{mm'}$ matrices parameterized from summation relations involving Slater integrals of atomic Hartree-Fock calculations.⁸⁰ This approach thus differs from the here-presented scheme, which does not rely on model systems like the free atom and includes intra-manifold screening effects, such as $t_{2g} \leftrightarrow e_g$.

The wide range of band gap values reported in both the theoretical and experimental literature underscores the pressing need for a more profound understanding of the insulating behavior of β -MnO₂. Considering the charge-transfer nature of the band gap and the coexistence of relatively localized and strongly hybridized states in both the Mn- d shell and the O- p shell, orbital-resolved DFT+ U calculations offer a promising starting point. In the interest of comparability, our calculations are carried out using a setup equivalent to that of Ref. 54, imposing the A1-AFM ordering in a $2 \times 2 \times 2$ supercell containing 48 atoms and considering once again different Hubbard manifolds.

Table 5: Comparison of equilibrium properties of A1-AFM β -MnO₂ obtained from PBEsol without and with various Hubbard corrections. U_1 and U_2 refer to various parameterizations of the PBEsol+ U approach, while V is the inter-site Hubbard parameter of the PBEsol+ U + V approach. a and c are the lattice parameters, V_0 is the unit cell volume, and E_g is the band gap value. All the presented results (including those from Ref. 54) were obtained using OAO projectors.

	PBEsol	+ $U_{t_{2g}}^{\text{Mn}}$	+ $U_{t_{2g}}^{\text{Mn}}$ + $U_{p_z}^{\text{O}}$	+ U^{Mn} (Ref. 54)	+ U^{Mn} + $V^{\text{Mn-O}}$ (Ref. 54)	Expt.
U_1 (eV)	—	1.59	1.64	6.34	6.76	—
U_2/V (eV)	—	—	4.62	—	(0.99, 1.10)	—
a (Å)	4.37	4.37	4.38	4.40	4.39	4.40 ¹⁴¹
c (Å)	2.83	2.86	2.88	2.94	2.92	2.88 ¹⁴¹
V_0 (Å ³)	54.68	54.64	55.26	57.07	56.35	55.79 ¹⁴¹
E_g (eV)	0.00	0.00	1.01	0.02	0.32	0.26, ¹³⁵ 1.50, ¹³⁷ 2.0 ¹³⁸

The first manifold solely considers the t_{2g} orbitals in order to single out the impact of the localized Mn- d states.⁶ As shown in Table 5, this correction only marginally influences

⁶Here, we use the t_{2g} irreducible representation in spite of the actual D_{4h} site symmetry of Mn⁴⁺ and therefore neglect the small energetic splitting between the A_{1g} , B_{1g} and B_{2g} representations.

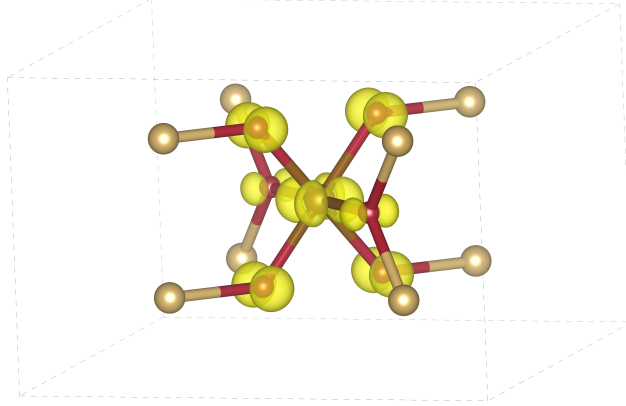


Figure 8: Isosurface plot of the highest fully occupied KS band of A1-AFM β -MnO₂ obtained using PBEsol+ $U_{t_{2g}}^{\text{Mn}}$, showing π interactions between O- p_z and Mn- t_{2g} orbitals. Mn atoms of opposite spin-polarization are colored dark and light brown, O atoms are red. For clarity, the interaction is only shown for one MnO₆ octahedron.

the band gap or the structural properties in comparison to bare PBEsol. This observation aligns with the modest value of $U_{t_{2g}}^{\text{Mn}} = 1.59$ eV, indicative of minimal local curvature due to the t_{2g} states. A much more significant improvement is achieved by considering the localized O- p_z orbitals (Figure 8). Correcting these states with a self-consistent Hubbard parameter $U_{p_z}^{\text{O}} = 4.62$ eV (in addition to the $U_{t_{2g}}^{\text{Mn}}$ correction) leads to an insulating gap of 1.01 eV. Moreover, the lattice parameters approach their experimental values, resulting in an error on the predicted cell volume smaller than 1%. Conversely, a shell-averaged U correction as large as 6.34 eV for Mn- d states only results in less accurate cell parameters and a still negligible band gap. This situation is only partly mended by the application of an additional inter-site V parameter.⁵⁴

The importance of including O- p_z in the Hubbard manifold is evidenced by the PDOS depicted in Figure 9. The states near the Fermi level exhibit notable O- p contributions, regardless of the correction applied. These contributions primarily stem from localized p_z orbitals, which engage in π interactions with the Mn- t_{2g} manifold (Figure 8). The other two p orbitals are subject to sp^2 hybridization and contribute to the formation of the lower-lying σ MOs in conjunction with Mn- e_g states. This observation underscores that applying shell-averaged U corrections to the entire O- p shell would weaken the σ bonds and lead to

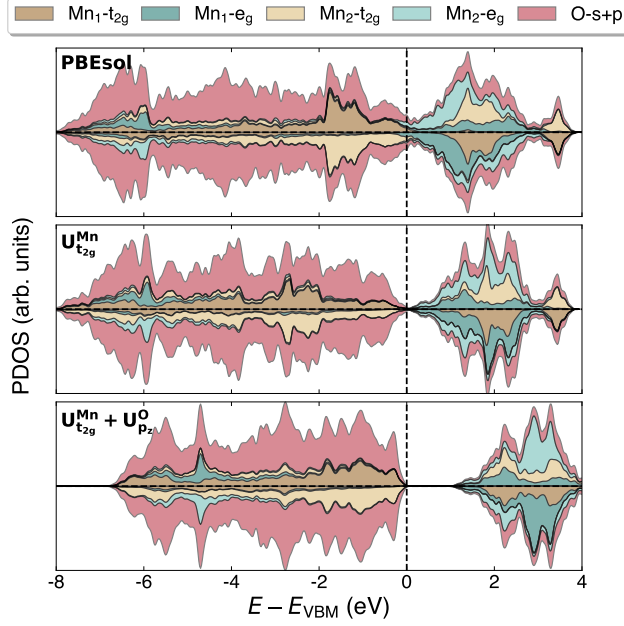


Figure 9: Stacked spin-resolved PDOS of the A1-AFM collinear ordering of β -MnO₂ computed with PBEsol and two types of orbital-resolved U corrections. Metallic behavior is observed when using PBEsol and PBEsol+ $U_{t_{2g}}^{\text{Mn}}$, whereas an insulating character is obtained with PBEsol+ $U_{t_{2g}}^{\text{Mn}} + U_{p_z}^{\text{O}}$. On each panel, the upper and lower subpanels correspond to the spin-up and spin-down channels, respectively.

Mn-O underbinding. For the same reason, applying corrections to the Mn- e_g states is neither required nor useful.

In conclusion, the orbital-resolved approach pinpoints deviations from PWL in the localized O- p_z orbitals as the potential root-cause of the absence of a band gap in β -MnO₂ when using DFT with semi-local functionals. This outcome underscores the frequently overlooked significance of ligand orbitals in electronic localization and establishes a foundation for future investigations. Again, achieving more comprehensive descriptions of this intricate charge-transfer insulator could entail incorporating the orbital-resolved U approach alongside inter-site V and unlike-spin Hund's J terms.

5 Outlook: orbital-resolved inter-site Hubbard interactions?

Hubbard U corrections are primarily designed to mitigate the FCE in KS states exhibiting strong atomic-like character, that is, at the on-site level. Orbitals involved in strong inter-atomic hybridization should not be corrected using U terms. This limitation is a consequence of the one-center projectors that are typically used to determine the occupation numbers for the Hubbard U energy functional, which inherently lack the ability to adequately represent localization on hybrid (i.e., molecular) orbitals. To counteract the FCE within covalent environments, the extended DFT+ U + V framework was introduced in Ref. 53, where conventional shell-averaged U corrections are augmented with an inter-site term scaled by a Hubbard parameter V in a way that restores ligand hybridization through two-center (dual) occupation numbers. However, although the + V correction often improves the predictions of electronic and structural properties compared to plain DFT+ U , the results presented for FeS₂ and MnO₂ exemplify that it only partially mitigates the impact of shell-averaged U corrections. Specifically, inter-site terms cannot rectify a substantial bias in the total energy arising from on-site terms since the values of U (for first-row TM elements) are typically between 4 and 10 eV, which is several times greater than typical values of V , which amount to ≈ 1 eV. For instance, the Hubbard U and V parameters of the strong-field molecular complex [Fe(CNH)₆]²⁺ from Sec. 4 are 8.42 (for Fe-3d states) and 1.12 eV (between Fe-3d and C-2p states) for the LS configuration, and 6.57 and 1.11 eV for the HS configuration, respectively. Applying these parameters, one obtains an adiabatic spin energy difference $\Delta E_{H-L} = -0.42$ eV that erroneously suggests a HS ground state for [Fe(CNH)₆]²⁺ (the CASPT2/CC reference is +2.82 eV, see Figure 6).

Given that the majority of spurious contributions to the total energy arise from the shell-averaged form of U , the implementation of orbital-resolved DFT+ U + V is an intriguing prospect, as already hinted in the concluding remarks of Ref. 53. This extension could ex-

ert precise control over electron localization on molecular orbitals, which could be achieved through individual Hubbard V_{ij}^{IJ} parameters. Moreover, such highly tailored but still fully first-principles corrections should allow to eliminate potential conflicts arising from the simultaneous treatment of orbitals by both U and V terms. With regard to the compounds discussed in the present work, the orbital-resolved U corrections of the localized t_g/t_{2g} orbitals could be augmented by V terms specific to the interaction of e_g with neighboring ligand orbitals. Note that orbital-resolved inter-site V parameters are readily obtained as a by-product of the calculation of U parameters within the generalized LR-cDFT approach. However, practical calculations with this fully-resolved approach would require the *a priori* assignment of two-center occupation numbers to specific MOs, which involves additional preparatory effort. Desirable will be the conception and implementation of appropriate automation workflows in supporting tools such as AiiDA.^{142,143} Alternatively, a simplified approach could involve using the Hubbard V correction in its current (averaged) form while retaining the orbital-dependence of U . This would serve as a pragmatic *ad-hoc* solution to the issues of U at the expense of consistency.

Another avenue for extension pertains to Hund’s J corrections, whose combination with the orbital-resolved U should be straightforward. Such ‘unlike-spin’ terms play a pivotal role in addressing the fractional spin error that occurs in systems characterized by significant magnetic coupling.^{50,62,75,84,132,144,145}

6 Conclusions

In this study, we have introduced an orbital-resolved generalization of the DFT+ U functional originally formulated by Dudarev et al.. Our implementation is agnostic about the specific nature of the Hubbard projectors employed and maintains full invariance against basis vector rotations. As a result, calculations involving forces and stresses require no adjustments stemming from this expansion. The true potential of the scheme emerges when the required

Hubbard parameters are derived from first principles. For this purpose, we have employed an adapted version of the LR-cDFT approach, enabling perturbative calculations with orbital resolution. This approach intrinsically incorporates intra-shell screening, which often causes orbital-resolved U parameters to be significantly smaller than their shell-averaged counterparts. Provided a proper selection of the target manifold, the orbital resolution therefore enables a more surgical use of DFT+ U that avoids overcorrections, as comparative calculations of six Fe(II) molecular hexacomplexes as well as of the charge-transfer insulators pyrite and pyrolusite underscore.

For instance, the orbital-resolved approach effectively addresses the bias in adiabatic spin energies towards HS states observed in shell-averaged DFT+ U .⁷⁶ Particularly noteworthy is its success in accurately predicting spin energies across a diverse spectrum of Fe(II) hexacomplexes, achieved through selective corrections of the highly localized t_{2g} orbitals. Explicit fractional charge calculations on $\text{Fe}[\text{CNH}]_6^{2+}$ suggest that these improvements are not coincidental: the orbital-resolved approach reliably counteracts the spurious global curvature of DFT with (semi-)local functionals with respect to the fractional addition or removal of electrons, reducing the FCE by an order of magnitude. In contrast, shell-averaged Hubbard U corrections exhibit a mixed performance: while they effectively diminish the FCE in the HS states, their efficacy wanes when addressing the LS states. Here, instead of rectifying the FCE, the convex error characteristic of (semi-)local DFT is converted into a comparably pronounced concave error. The results also suggest that a sole correction of the localized t_{2g} orbitals performs slightly better than a joint correction of t_{2g} and the rather hybridized e_g manifold, even when using orbital-resolved U parameters. The superiority of the orbital-resolved formulation over the shell-averaged approximation also extends to the charge-transfer insulators FeS_2 and $\beta\text{-MnO}_2$. The correct non-magnetic ground state of the former is only stabilized when orbital-resolved Hubbard parameters are used. The magnitude of the large experimental band gap of the latter can only be achieved by applying a pinpointed Hubbard correction to the frontier O- p_z orbitals, whereas standard Hubbard U

corrections to the d shell of Mn fail to open a significant band gap.

As these examples illustrate, the success of the orbital-resolved formulation predominantly originates from the exclusion of hybridized orbitals from the Hubbard manifold. From a theoretical perspective, the necessity to exclude hybridized orbitals is rooted in the very definition of U as an *on-site* term. However, practically implementing this definition poses challenges, particularly given that many DFT+ U investigations rely on atomic-like orbitals as Hubbard projectors. This approach can lead to occupancy eigenvalues far from 0 or 1, especially in compounds featuring covalent bonds. These fractional values, however, are not related to the electron self-interaction, as they arise from a one-center projector being applied to a two-center phenomenon, namely a molecular orbital. In such scenarios, the orbital-resolved approach provides an *ad-hoc* solution that allows to circumvent the potential conflict of on-site corrections with the intricacies of covalently bonded systems.

In a broader context, it is crucial to emphasize that the refined approach presented in this work constitutes just one among various potent (Hubbard) corrections available to DFT. As such, its effectiveness and ability to achieve consistent enhancements relies on a thoughtful and technically well-executed application. In practical terms, this is achieved by adopting a more nuanced strategy for the determination of Hubbard manifolds, tailored to the specific Hubbard projectors employed. Such a strategy should consider *localized* ligand orbitals for Hubbard corrections in situations where these act as frontier states. In addition, it might be desirable to address the FCE in hybrid (i.e., molecular) orbitals. For this purpose, the use of Wannier functions as Hubbard projectors or the adoption of an extended orbital-resolved DFT+ U + V approach should be contemplated. A pivotal aspect of our future investigations will focus on developing a protocol to automate the choice of Hubbard manifolds based on measurable criteria. This step aims to streamline and standardize the approach’s application, ensuring its systematic and effective use across diverse systems and scenarios.

Acknowledgement

We thank Louis Ponet for fruitful discussions. EM was funded by the Deutsche Forschungsgemeinschaft (DFG, German Research Foundation) – Project No. 286518848 – RTG 2247 QM³. IT and NM acknowledge support from the Swiss National Science Foundation (SNSF) through its National Centre of Competence in Research (NCCR) MARVEL (Grant No. 205602). NM acknowledges funding from the U Bremen Excellence Chair programme. The authors also acknowledge the computing time granted by the Resource Allocation Board and provided on the supercomputers Lise and Emmy at NHR@ZIB and NHR@Göttingen as part of the NHR infrastructure (project hbc00053) and the Swiss National Supercomputing Centre (CSCS) under project No. s1073.

Supporting Information Available

Shifts of VBM and CBM KS eigenvalues in pyrite due to Hubbard corrections.

References

- (1) Hohenberg, P.; Kohn, W. Inhomogeneous Electron Gas. *Phys. Rev.* **1964**, *136*, B864–B871.
- (2) Kohn, W.; Sham, L. J. Self-Consistent Equations Including Exchange and Correlation Effects. *Phys. Rev.* **1965**, *140*, A1133–A1138.
- (3) Hubbard, J. Electron correlations in narrow energy bands. *Proc. R. Soc. A: Math. Phys.* **1963**, *276*, 238–257.
- (4) Anisimov, V.; Zaanen, J.; Andersen, O. Band theory and Mott insulators: Hubbard U instead of Stoner I . *Phys. Rev. B* **1991**, *44*, 943.

- (5) Anisimov, V. I.; Solovyev, I. V.; Korotin, M. A.; Czyżyk, M. T.; Sawatzky, G. A. Density-functional theory and NiO photoemission spectra. *Phys. Rev. B* **1993**, *48*, 16929–16934.
- (6) Liechtenstein, A. I.; Anisimov, V. I.; Zaanen, J. Density-functional theory and strong interactions: Orbital ordering in Mott-Hubbard insulators. *Phys. Rev. B* **1995**, *52*, R5467–R5470.
- (7) Cococcioni, M. A LDA+U Study of Selected Iron Compounds. Ph.D. thesis, International School for Advanced Studies (SISSA), Trieste, 2002.
- (8) Cococcioni, M.; de Gironcoli, S. Linear response approach to the calculation of the effective interaction parameters in the LDA + U method. *Phys. Rev. B* **2005**, *71*, 035105.
- (9) Dudarev, S. L.; Botton, G. A.; Savrasov, S. Y.; Humphreys, C. J.; Sutton, A. P. Electron-energy-loss spectra and the structural stability of nickel oxide: An LSDA+U study. *Phys. Rev. B* **1998**, *57*, 1505–1509.
- (10) Perdew, J. P.; Parr, R. G.; Levy, M.; Balduz, J. L. Density-Functional Theory for Fractional Particle Number: Derivative Discontinuities of the Energy. *Phys. Rev. Lett.* **1982**, *49*, 1691–1694.
- (11) Yang, W.; Zhang, Y.; Ayers, P. W. Degenerate Ground States and a Fractional Number of Electrons in Density and Reduced Density Matrix Functional Theory. *Phys. Rev. Lett.* **2000**, *84*, 5172–5175.
- (12) Kulik, H. J.; Cococcioni, M.; Scherlis, D. A.; Marzari, N. Density Functional Theory in Transition-Metal Chemistry: A Self-Consistent Hubbard U Approach. *Phys. Rev. Lett.* **2006**, *97*, 103001.

- (13) Zhao, Q.; Kulik, H. J. Where Does the Density Localize in the Solid State? Divergent Behavior for Hybrids and DFT+U. *J. Chem. Theory Comput.* **2018**, *14*, 670–683.
- (14) Levy, M. Electron densities in search of Hamiltonians. *Phys. Rev. A* **1982**, *26*, 1200–1208.
- (15) Zhao, Q.; Ioannidis, E. I.; Kulik, H. J. Global and local curvature in density functional theory. *J. Chem. Phys.* **2016**, *145*, 054109.
- (16) Dabo, I.; Ferretti, A.; Poilvert, N.; Li, Y.; Marzari, N.; Cococcioni, M. Koopmans’ Condition for Density-Functional Theory. *Phys. Rev. B* **2010**, *82*, 115121.
- (17) Borghi, G.; Ferretti, A.; Nguyen, N. L.; Dabo, I.; Marzari, N. Koopmans-Compliant Functionals and Their Performance against Reference Molecular Data. *Phys. Rev. B* **2014**, *90*, 075135.
- (18) Wang, L.; Maxisch, T.; Ceder, G. Oxidation energies of transition metal oxides within the GGA+U framework. *Phys. Rev. B* **2006**, *73*, 195107.
- (19) Le Bacq, O.; Pasturel, A.; Bengone, O. Impact on electronic correlations on the structural stability, magnetism, and voltage of LiCoPO₄ battery. *Phys. Rev. B* **2004**, *69*, 245107.
- (20) Aykol, M.; Wolverton, C. Local environment dependent GGA+U method for accurate thermochemistry of transition metal compounds. *Phys. Rev. B* **2014**, *90*, 115105.
- (21) Isaacs, E.; Marianetti, C. Compositional phase stability of strongly correlated electron materials within DFT+U. *Phys. Rev. B* **2017**, *95*, 045141.
- (22) Dederichs, P. H.; Blügel, S.; Zeller, R.; Akai, H. Ground States of Constrained Systems: Application to Cerium Impurities. *Phys. Rev. Lett.* **1984**, *53*, 2512–2515.
- (23) McMahan, A.; Martin, R.; Satpathy, S. Calculated effective Hamiltonian for La₂CuO₄ and solution in the impurity Anderson approximation. *Phys. Rev. B* **1988**, *38*, 6650.

- (24) Gunnarsson, O.; Andersen, O.; Jepsen, O.; Zaanen, J. Density-functional calculation of the parameters in the Anderson model: Application to Mn in CdTe. *Phys. Rev. B* **1989**, *39*, 1708.
- (25) Hybertsen, M.; Schlüter, M.; Christensen, N. Calculation of Coulomb-interaction parameters for La_2CuO_4 using a constrained-density-functional approach. *Phys. Rev. B* **1989**, *39*, 9028.
- (26) Gunnarsson, O. Calculation of parameters in model Hamiltonians. *Phys. Rev. B* **1990**, *41*, 514.
- (27) Pickett, W. E.; Erwin, S. C.; Ethridge, E. C. Reformulation of the LDA + U method for a local-orbital basis. *Phys. Rev. B* **1998**, *58*, 1201–1209.
- (28) Solovyev, I.; Imada, M. Screening of Coulomb interactions in transition metals. *Phys. Rev. B* **2005**, *71*, 045103.
- (29) Nakamura, K.; Arita, R.; Yoshimoto, Y.; Tsuneyuki, S. First-principles calculation of effective onsite Coulomb interactions of 3d transition metals: Constrained local density functional approach with maximally localized Wannier functions. *Phys. Rev. B* **2006**, *74*, 235113.
- (30) Shishkin, M.; Sato, H. Self-consistent parametrization of DFT + U framework using linear response approach: Application to evaluation of redox potentials of battery cathodes. *Phys. Rev. B* **2016**, *93*, 085135.
- (31) Springer, M.; Aryasetiawan, F. Frequency-dependent screened interaction in Ni within the random-phase approximation. *Phys. Rev. B* **1998**, *57*, 4364.
- (32) Kotani, T. *Ab initio* random-phase-approximation calculation of the frequency-dependent effective interaction between 3d electrons: Ni, Fe, and MnO. *J. Phys. Condens. Matter* **2000**, *12*, 2413.

- (33) Aryasetiawan, F.; Imada, M.; Georges, A.; Kotliar, G.; Biermann, S.; Lichtenstein, A. I. Frequency-dependent local interactions and low-energy effective models from electronic structure calculations. *Phys. Rev. B* **2004**, *70*, 195104.
- (34) Aryasetiawan, F.; Karlsson, K.; Jepsen, O.; Scönberger, U. Calculations of Hubbard U from first-principles. *Phys. Rev. B* **2006**, *74*, 125106.
- (35) Karlsson, K.; Aryasetiawan, F.; Jepsen, O. Method for calculating the electronic structure of correlated materials from a truly first-principles LDA + U scheme. *Phys. Rev. B* **2010**, *81*, 245113.
- (36) Mosey, N. J.; Carter, E. A. *Ab initio* evaluation of Coulomb and exchange parameters for DFT + U calculations. *Phys. Rev. B* **2007**, *76*, 155123.
- (37) Mosey, N. J.; Liao, P.; Carter, E. A. Rotationally invariant *ab initio* evaluation of Coulomb and exchange parameters for DFT+ U calculations. *J. Chem. Phys.* **2008**, *129*, 014103.
- (38) Andriotis, A.; Sheetz, R.; Menon, M. LSDA+ U method: A calculation of the U values at the Hartree-Fock level of approximation. *Phys. Rev. B* **2010**, *81*, 245103.
- (39) Agapito, L.; Curtarolo, S.; Buongiorno Nardelli, M. Reformulation of DFT+ U as a Pseudohybrid Hubbard Density Functional for Accelerated Materials Discovery. *Phys. Rev. X* **2015**, *5*, 011006.
- (40) Tancogne-Dejean, N.; Rubio, A. Parameter-free hybridlike functional based on an extended Hubbard model: DFT+ U + V . *Phys. Rev. B* **2020**, *102*, 155117.
- (41) Lee, S.-H.; Son, Y.-W. First-principles approach with a pseudohybrid density functional for extended Hubbard interactions. *Phys. Rev. Res.* **2020**, *2*, 043410.
- (42) Cococcioni, M.; Marzari, N. Energetics and cathode voltages of Li M PO 4 olivines

- (M = Fe , Mn) from extended Hubbard functionals. *Phys. Rev. Materials* **2019**, *3*, 033801.
- (43) Ricca, C.; Timrov, I.; Cococcioni, M.; Marzari, N.; Aschauer, U. Self-consistent site-dependent DFT+*U* study of stoichiometric and defective SrMnO₃. *Phys. Rev. B* **2019**, *99*, 094102.
- (44) Sun, Y.; Cococcioni, M.; Wentzcovitch, R. *Phys. Rev. Mater.* **2020**, *4*, 063605.
- (45) Kirchner-Hall, N. E.; Zhao, W.; Xiong, Y.; Timrov, I.; Dabo, I. Extensive Benchmarking of DFT+*U* Calculations for Predicting Band Gaps. *Appl. Sci.* **2021**, *11*, 2395.
- (46) Xiong, Y.; Campbell, Q.; Fanghanel, J.; Badding, C.; Wang, H.; Kirchner-Hall, N.; Theibault, M.; Timrov, I.; Mondschein, J.; Seth, K.; Katz, R.; Molina Villarino, A.; Pamuk, B.; Penrod, M.; Khan, M.; Rivera, T.; Smith, N.; Quintana, X.; Orbe, P.; Fennie, C.; Asem-Hiablie, S.; Young, J.; Deutsch, T.; Cococcioni, M.; Gopalan, V.; Abruña, H.; Schaak, R.; Dabo, I. Optimizing accuracy and efficacy in data-driven materials discovery for the solar production of hydrogen. *Energy Environ. Sci.* **2021**, *14*, 2335.
- (47) Zhou, J.-J.; Park, J.; Timrov, I.; Floris, A.; Cococcioni, M.; Marzari, N.; Bernardi, M. Ab Initio Electron-Phonon Interactions in Correlated Electron Systems. *Phys. Rev. Lett.* **2021**, *127*, 126404.
- (48) Moore, G. C.; Horton, M. K.; Ganose, A. M.; Siron, M.; Linscott, E.; O'Regan, D. D.; Persson, K. A. High-throughput determination of Hubbard *U* and Hund *J* values for transition metal oxides via linear response formalism. 2022; <http://arxiv.org/abs/2201.04213>, arXiv:2201.04213.
- (49) Haddadi, F.; Linscott, E.; Timrov, I.; Marzari, N.; Gibertini, M. On-Site and Inter-Site Hubbard Corrections in Magnetic Monolayers: The Case of FePS₃ and CrI₃. 2023; <http://arxiv.org/abs/2306.06286>, arXiv:2201.04213.

- (50) Linscott, E. B.; Cole, D. J.; Payne, M. C.; O'Regan, D. D. Role of spin in the calculation of Hubbard U and Hund's J parameters from first principles. *Phys. Rev. B* **2018**, *98*, 235157.
- (51) Timrov, I.; Marzari, N.; Cococcioni, M. Hubbard parameters from density-functional perturbation theory. *Phys. Rev. B* **2018**, *98*, 085127.
- (52) Timrov, I.; Marzari, N.; Cococcioni, M. Self-consistent Hubbard parameters from density-functional perturbation theory in the ultrasoft and projector-augmented wave formulations. *Phys. Rev. B* **2021**, *103*, 045141.
- (53) Leiria Campo Jr, V.; Cococcioni, M. Extended DFT + U + V method with on-site and inter-site electronic interactions. *J. Phys. Condens. Matter* **2010**, *22*, 055602.
- (54) Mahajan, R.; Timrov, I.; Marzari, N.; Kashyap, A. Importance of intersite Hubbard interactions in beta - MnO₂ : A first-principles DFT+U+V study. *Phys. Rev. Mater.* **2021**, *5*, 104402.
- (55) O'Regan, D. D.; Hine, N. D. M.; Payne, M. C.; Mostofi, A. A. Projector self-consistent DFT + U using nonorthogonal generalized Wannier functions. *Phys. Rev. B* **2010**, *82*, 081102.
- (56) Kulik, H. J.; Marzari, N. A self-consistent Hubbard U density-functional theory approach to the addition-elimination reactions of hydrocarbons on bare FeO⁺. *J. Chem. Phys.* **2008**, *129*, 134314.
- (57) Kraisler, E.; Kronik, L. Piecewise Linearity of Approximate Density Functionals Revisited: Implications for Frontier Orbital Energies. *Phys. Rev. Lett.* **2013**, *110*, 126403.
- (58) Linscott, E. B.; Colonna, N.; De Gennaro, R.; Nguyen, N. L.; Borghi, G.; Ferretti, A.; Dabo, I.; Marzari, N. Koopmans : An Open-Source Package for Accurately and Effi-

- ciently Predicting Spectral Properties with Koopmans Functionals. *J. Chem. Theory Comput.* **2023**, *19*, 7097–7111.
- (59) Nguyen, N. L.; Colonna, N.; Ferretti, A.; Marzari, N. Koopmans-Compliant Spectral Functionals for Extended Systems. *Phys. Rev. X* **2018**, *8*, 021051.
- (60) Himmetoglu, B.; Floris, A.; de Gironcoli, S.; Cococcioni, M. Hubbard-corrected DFT energy functionals: The LDA+U description of correlated systems. *Int. J. Quantum Chem.* **2014**, *114*, 14–49.
- (61) May, K. J.; Kolpak, A. M. Improved description of perovskite oxide crystal structure and electronic properties using self-consistent Hubbard U corrections from ACBN0. *Phys. Rev. B* **2020**, *101*, 165117.
- (62) Orhan, O. K.; O’Regan, D. D. First-principles Hubbard U and Hund’s J corrected approximate density functional theory predicts an accurate fundamental gap in rutile and anatase TiO₂. *Phys. Rev. B* **2020**, *101*, 245137.
- (63) Gelin, S.; Kirchner-Hall, N.; Katzbaer, R.; Theibault, M.; Xiong, Y.; Zhao, W.; Khan, M.; Andrewlavage, E.; Orbe, P.; Baksa, S.; Cococcioni, M.; Timrov, I.; Campbell, Q.; Abruna, H.; Schaak, R.; Dabo, I. Ternary oxides of *s*- and *p*-block metals for photocatalytic solar-to-hydrogen conversion. *arXiv:2303.03332*
- (64) Timrov, I.; Agrawal, P.; Zhang, X.; Erat, S.; Liu, R.; Braun, A.; Cococcioni, M.; Caltandra, M.; Marzari, N.; Passerone, D. Electronic structure of Ni-substituted LaFeO₃ from near edge x-ray absorption fine structure experiments and first-principles simulations. *Phys. Rev. Res.* **2020**, *2*, 033265.
- (65) Ricca, C.; Timrov, I.; Cococcioni, M.; Marzari, N.; Aschauer, U. Self-consistent DFT+*U*+*V* study of oxygen vacancies in SrTiO₃. *Phys. Rev. Res.* **2020**, *2*, 023313.

- (66) Floris, A.; Timrov, I.; Himmetoglu, B.; Marzari, N.; de Gironcoli, S.; Cococcioni, M. Hubbard-corrected density functional perturbation theory with ultrasoft pseudopotentials. *Phys. Rev. B* **2020**, *101*, 064305.
- (67) Timrov, I.; Aquilante, F.; Cococcioni, M.; Marzari, N. Accurate Electronic Properties and Intercalation Voltages of Olivine-Type Li-Ion Cathode Materials from Extended Hubbard Functionals. *PRX Energy* **2022**, *1*, 033003.
- (68) Kulik, H. J.; Marzari, N. Transition-metal dioxides: A case for the intersite term in Hubbard-model functionals. *J. Chem. Phys.* **2011**, *134*, 094103.
- (69) Mahajan, R.; Kashyap, A.; Timrov, I. Pivotal Role of Intersite Hubbard Interactions in Fe-Doped α -MnO₂. *J. Phys. Chem. C* **2022**, *126*, 14353–14365.
- (70) Timrov, I.; Kotiuga, M.; Marzari, N. Unraveling the effects of inter-site Hubbard interactions in spinel Li-ion cathode materials. *Phys. Chem. Chem. Phys.* **2023**, *25*, 9061.
- (71) Binci, L.; Kotiuga, M.; Timrov, I.; Marzari, N. Hybridization driving distortions and multiferroicity in rare-earth nickelates. *Phys. Rev. Research* **2023**, *5*, 033146.
- (72) Bonfá, P.; Onuorah, I.; Lang, F.; Timrov, I.; Monacelli, L.; Wang, C.; Sun, X.; Petravic, O.; Pizzi, G.; Marzari, N.; Blundell, S.; De Renzi, R. Magnetostriction-driven muon localisation in an antiferromagnetic oxide. *arXiv:2305.12237*
- (73) Gebreyesus, G.; Bastonero, L.; Kotiuga, M.; Marzari, N.; Timrov, I. Understanding the role of Hubbard corrections in the rhombohedral phase of BaTiO₃. *arXiv:2309.04348*
- (74) Shishkin, M.; Sato, H. Challenges in computational evaluation of redox and magnetic properties of Fe-based sulfate cathode materials of Li- and Na-ion batteries. *J. Phys. Condens. Matter* **2017**, *29*, 215701.

- (75) Shishkin, M.; Sato, H. Evaluation of redox potentials of cathode materials of alkali-ion batteries using extended DFT+ $U+U$ up/down method: The role of interactions between the electrons with opposite spins. *J. Chem. Phys.* **2021**, *154*, 114709.
- (76) Mariano, L. A.; Vlasisavljevich, B.; Poloni, R. Biased Spin-State Energetics of Fe(II) Molecular Complexes within Density-Functional Theory and the Linear-Response Hubbard U Correction. *J. Chem. Theory Comput.* **2020**, *16*, 6755–6762.
- (77) Mariano, L. A.; Vlasisavljevich, B.; Poloni, R. Improved Spin-State Energy Differences of Fe(II) Molecular and Crystalline Complexes *via* the Hubbard U -Corrected Density. *J. Chem. Theory Comput.* **2021**, *17*, 2807–2816.
- (78) O'Regan, D. D. *Optimised Projections for the Ab Initio Simulation of Large and Strongly Correlated Systems*; Springer Berlin Heidelberg: Berlin, Heidelberg, 2012; pp 89–123.
- (79) Solovyev, I.; Hamada, N.; Terakura, K. t_{23} versus all $3d$ localization in LaMO₃ perovskites (M =Ti–Cu): First-principles study. *Phys. Rev. B* **1996**, *53*, 7158–7170.
- (80) Czyżyk, M. T.; Sawatzky, G. A. Local-density functional and on-site correlations: The electronic structure of La₂CuO₄ and LaCuO₃. *Phys. Rev. B* **1994**, *49*, 14211–14228.
- (81) Ylvisaker, E. R.; Pickett, W. E.; Koepernik, K. Anisotropy and magnetism in the LSDA + U method. *Phys. Rev. B* **2009**, *79*, 035103.
- (82) Kasinathan, D.; Koepernik, K.; Pickett, W. E. Pressure-driven magnetic moment collapse in the ground state of MnO. *New Journal of Physics* **2007**, *9*, 235–235.
- (83) Tompsett, D. A.; Middlemiss, D. S.; Islam, M. S. Importance of Anisotropic Coulomb Interactions and Exchange to the Band Gap and Antiferromagnetism of beta-MnO₂ from DFT+ U . *Phys. Rev. B* **2012**, *86*, 205126.

- (84) Shishkin, M.; Sato, H. DFT+ U in Dudarev’s formulation with corrected interactions between the electrons with opposite spins: The form of Hamiltonian, calculation of forces, and bandgap adjustments. *J. Chem. Phys.* **2019**, *151*, 024102.
- (85) Georges, A.; Kotliar, G.; Krauth, W.; Rozenberg, M. J. Dynamical mean-field theory of strongly correlated fermion systems and the limit of infinite dimensions. *Rev. Mod. Phys.* **1996**, *68*, 13–125.
- (86) Vaugier, L.; Jiang, H.; Biermann, S. Hubbard U and Hund exchange J in transition metal oxides: Screening versus localization trends from constrained random phase approximation. *Phys. Rev. B* **2012**, *86*, 165105.
- (87) Hampel, A.; Lee-Hand, J.; Georges, A.; Dreyer, C. E. Correlation-induced octahedral rotations in SrMoO₃. *Phys. Rev. B* **2021**, *104*, 035102.
- (88) Merkel, M. E.; Ederer, C. Calculation of Screened Coulomb Interaction Parameters for the Charge-Disproportionated Insulator CaFeO₃. 2023; arXiv:2310.16541.
- (89) Prentice, J. C. A.; Aarons, J.; Womack, J. C.; Allen, A. E. A.; Andrinopoulos, L.; Anton, L.; Bell, R. A.; Bhandari, A.; Bramley, G. A.; Charlton, R. J.; Clements, R. J.; Cole, D. J.; Constantinescu, G.; Corsetti, F.; Dubois, S. M.-M.; Duff, K. K. B.; Escartín, J. M.; Greco, A.; Hill, Q.; Lee, L. P.; Linscott, E.; O’Regan, D. D.; Phipps, M. J. S.; Ratcliff, L. E.; Serrano, A. R.; Tait, E. W.; Teobaldi, G.; Vitale, V.; Yeung, N.; Zuehlsdorff, T. J.; Dziedzic, J.; Haynes, P. D.; Hine, N. D. M.; Mostofi, A. A.; Payne, M. C.; Skylaris, C.-K. The ONETEP linear-scaling density functional theory program. *J. Chem. Phys.* **2020**, *152*, 174111.
- (90) Kulik, H. J. Perspective: Treating electron over-delocalization with the DFT+ U method. *J. Chem. Phys.* **2015**, *142*, 240901.
- (91) Timrov, I.; Aquilante, F.; Binci, L.; Cococcioni, M.; Marzari, N. Pulay forces in

- density-functional theory with extended Hubbard functionals: From nonorthogonalized to orthogonalized manifolds. *Phys. Rev. B* **2020**, *102*, 235159.
- (92) Kulik, H. J.; Seelam, N.; Mar, B. D.; Martínez, T. J. Adapting DFT+ U for the Chemically Motivated Correction of Minimal Basis Set Incompleteness. *J. Phys. Chem. A* **2016**, *120*, 5939–5949.
- (93) Rohrbach, A.; Hafner, J.; Kresse, G. Molecular adsorption on the surface of strongly correlated transition-metal oxides: A case study for CO/NiO(100). *Phys. Rev. B* **2004**, *69*, 075413.
- (94) Nawa, K.; Akiyama, T.; Ito, T.; Nakamura, K.; Oguchi, T.; Weinert, M. Scaled effective on-site Coulomb interaction in the DFT+ U method for correlated materials. *Phys. Rev. B* **2018**, *97*, 035117.
- (95) Löwdin, P. On the Non-Orthogonality Problem Connected with the Use of Atomic Wave Functions in the Theory of Molecules and Crystals. *J. Chem. Phys.* **1950**, *18*, 365–375.
- (96) Korotin, D.; Kukolev, V.; Kozhevnikov, A.; Novoselov, D.; Anisimov, V. Electronic correlations and crystal structure distortions in BaBiO₃. *J. Phys. Condens. Matter* **2012**, *24*, 415603.
- (97) Novoselov, D.; Korotin, D.; Anisimov, V. Hellmann-Feynman forces within the DFT+ U in Wannier functions basis. *J. Phys. Condens. Matter* **2015**, *27*, 325602.
- (98) Marzari, N.; Vanderbilt, D. Maximally localized generalized Wannier functions for composite energy bands. *Phys. Rev. B* **1997**, *56*, 12847–12865.
- (99) Marzari, N.; Mostofi, A.; Yates, J.; Souza, I.; Vanderbilt, D. Maximally localized Wannier functions: Theory and applications. *Rev. Mod. Phys.* **2012**, *84*, 1419–1475.

- (100) Qiao, J.; Pizzi, G.; Marzari, N. Automated mixing of maximally localized Wannier functions into target manifolds. *npj Comp. Mater.* **2023**, *9*.
- (101) Tesch, R.; Kowalski, P. M. Hubbard U parameters for transition metals from first principles. *Phys. Rev. B* **2022**, *105*, 195153.
- (102) Sakuma, R.; Aryasetiawan, F. First-principles calculations of dynamical screened interactions for the transition metal oxides MO (M=Mn, Fe, Co, Ni). *Phys. Rev. B* **2013**, *87*, 165118.
- (103) Timrov, I.; Marzari, N.; Cococcioni, M. HP – A code for the calculation of Hubbard parameters using density-functional perturbation theory. *Comput. Phys. Commun.* **2022**, *279*, 108455.
- (104) Kulik, H. J.; Marzari, N. Systematic study of first-row transition-metal diatomic molecules: A self-consistent DFT+U approach. *J. Chem. Phys.* **2010**, *133*, 114103.
- (105) Yu, K.; Carter, E. Communication: Comparing ab initio methods of obtaining effective U parameters for closed-shell materials. *J. Chem. Phys.* **2014**, *140*, 121105.
- (106) Giannozzi, P.; Baroni, S.; Bonini, N.; Calandra, M.; Car, R.; Cavazzoni, C.; Ceresoli, D.; Chiarotti, G.; Cococcioni, M.; Dabo, I.; Dal Corso, A.; De Gironcoli, S.; Fabris, S.; Fratesi, G.; Gebauer, R.; Gerstmann, U.; Gougoussis, C.; Kokalj, A.; Lazzeri, M.; Martin-Samos, L.; Marzari, N.; Mauri, F.; Mazzarello, R.; Paolini, S.; Pasquarello, A.; Paulatto, L.; Sbraccia, C.; Scandolo, S.; Sclauzero, G.; Seitsonen, A.; Smogunov, A.; Umari, P.; Wentzcovitch, R. Quantum ESPRESSO: A modular and open-source software project for quantum simulations of materials. *J. Phys. Condens. Matter* **2009**, *21*, 395502.
- (107) Giannozzi, P.; Andreussi, O.; Brumme, T.; Bunau, O.; Buongiorno Nardelli, M.; Calandra, M.; Car, R.; Cavazzoni, C.; Ceresoli, D.; Colonna, N.;

- Carnimeo, I.; Dal Corso, A.; de Gironcoli, S.; Delugas, P.; DiStasio Jr., R. A.; Ferretti, A.; Floris, A.; Fratesi, G.; Fugallo, G.; Gebauer, R.; Gerstmann, U.; Giustino, F.; Gorni, T.; Jia, J.; Kawamura, M.; Ko, H.-Y.; Kokalj, A.; Küçükbenli, E.; Lazzeri, M.; Marsili, M.; Marzari, N.; Mauri, F.; Nguyen, N. L.; Nguyen, H.-V.; Otero-de-la Rosa, A.; Paulatto, L.; Poncé, S.; Rocca, D.; Sabatini, R.; Santra, B.; Schlipf, M.; Seitsonen, A.; Smogunov, A.; Timrov, I.; Thonhauser, T.; Umari, P.; Vast, N.; Baroni, S. Advanced capabilities for materials modelling with Quantum ESPRESSO. *J. Phys. Condens. Matter* **2017**, *29*, 465901.
- (108) Giannozzi, P.; Barone, O.; Bonfà, P.; Brunato, D.; Car, R.; Carnimeo, I.; Cavazzoni, C.; de Gironcoli, S.; Delugas, P.; Ferrari Ruffino, F.; Ferretti, A.; Marzari, N.; Timrov, I.; Urru, A.; Baroni, S. Quantum ESPRESSO toward the exascale. *J. Chem. Phys.* **2020**, *152*, 154105.
- (109) Momma, K.; Izumi, F. VESTA for Three-Dimensional Visualization of Crystal, Volumetric and Morphology Data. *J. Appl. Crystallogr.* **2011**, *44*, 1272–1276.
- (110) Fletcher, R. *Practical Methods of Optimization*, 2nd ed.; Wiley: Chichester, 1987.
- (111) Perdew, J. P.; Burke, K.; Ernzerhof, M. Generalized Gradient Approximation Made Simple. *Phys. Rev. Lett.* **1996**, *77*, 3865–3868.
- (112) Küçükbenli, E.; Monni, M.; Adetunji, B. I.; Ge, X.; Adebayo, G. A.; Marzari, N.; de Gironcoli, S.; Corso, A. D. Projector augmented-wave and all-electron calculations across the periodic table: a comparison of structural and energetic properties. 2014; <http://arxiv.org/abs/1404.3015>, arXiv:1404.3015.
- (113) Garrity, K. F.; Bennett, J. W.; Rabe, K. M.; Vanderbilt, D. Pseudopotentials for high-throughput DFT calculations. *Comput. Mater. Sci.* **2014**, *81*, 446–452.
- (114) Dal Corso, A. Pseudopotentials periodic table: From H to Pu. *Comput. Mater. Sci.* **2014**, *95*, 337–350.

- (115) Lejaeghere, K.; Bihlmayer, G.; Björkman, T.; Blaha, P.; Blügel, S.; Blum, V.; Caliste, D.; Castelli, I. E.; Clark, S. J.; Dal Corso, A.; de Gironcoli, S.; Deutsch, T.; Dewhurst, J. K.; Di Marco, I.; Draxl, C.; Duřak, M.; Eriksson, O.; Flores-Livas, J. A.; Garrity, K. F.; Genovese, L.; Giannozzi, P.; Giantomassi, M.; Goedecker, S.; Gonze, X.; Grånäs, O.; Gross, E. K. U.; Gulans, A.; Gygi, F.; Hamann, D. R.; Hasnip, P. J.; Holzwarth, N. A. W.; Iuřan, D.; Jochym, D. B.; Jollet, F.; Jones, D.; Kresse, G.; Koepernik, K.; Küçükbenli, E.; Kvashnin, Y. O.; Loch, I. L. M.; Lubeck, S.; Marsman, M.; Marzari, N.; Nitzsche, U.; Nordström, L.; Ozaki, T.; Paulatto, L.; Pickard, C. J.; Poelmans, W.; Probert, M. I. J.; Refson, K.; Richter, M.; Rignanese, G.-M.; Saha, S.; Scheffler, M.; Schlipf, M.; Schwarz, K.; Sharma, S.; Tavazza, F.; Thunström, P.; Tkatchenko, A.; Torrent, M.; Vanderbilt, D.; van Setten, M. J.; Van Speybroeck, V.; Wills, J. M.; Yates, J. R.; Zhang, G.-X.; Cottenier, S. Reproducibility in density functional theory calculations of solids. *Science* **2016**, *351*.
- (116) Prandini, G.; Marrazzo, A.; Castelli, I. E.; Mounet, N.; Marzari, N. Precision and efficiency in solid-state pseudopotential calculations. *Npj Comput. Mater.* **2018**, *4*, 72.
- (117) Moynihan, G.; Teobaldi, G.; O'Regan, D. D. A self-consistent ground-state formulation of the first-principles Hubbard U parameter validated on one-electron self-interaction error. 2017; <http://arxiv.org/abs/1704.08076>, arXiv:1704.08076.
- (118) Zuñiga-Puelles, E.; Cardoso-Gil, R.; Bobnar, M.; Veremchuk, I.; Himcinschi, C.; Hennig, C.; Kortus, J.; Heide, G.; Gumeniuk, R. Structural stability and thermoelectric performance of high quality synthetic and natural pyrites (FeS₂). *Dalton Trans.* **2019**, *48*, 10703–10713.
- (119) Banjara, D.; Malozovsky, Y.; Franklin, L.; Bagayoko, D. First-principles studies of electronic, transport and bulk properties of pyrite FeS₂. *AIP Advances* **2018**, *8*, 025212.

- (120) Sun, R.; Chan, M. K. Y.; Ceder, G. First-principles electronic structure and relative stability of pyrite and marcasite: Implications for photovoltaic performance. *Phys. Rev. B* **2011**, *83*, 235311.
- (121) Eyert, V.; Höck, K.-H.; Fiechter, S.; Tributsch, H. Electronic structure of FeS₂: The crucial role of electron-lattice interaction. *Phys. Rev. B* **1998**, *57*, 6350–6359.
- (122) Armiento, R.; Mattsson, A. E. Functional designed to include surface effects in self-consistent density functional theory. *Phys. Rev. B* **2005**, *72*, 085108.
- (123) Burns, G. *Introduction to group theory with applications*; Materials science and technology; Academic Press: New York, 1977.
- (124) Schena, T.; Bihlmayer, G.; Blügel, S. First-principles studies of FeS₂ using many-body perturbation theory in the G₀W₀ approximation. *Phys. Rev. B* **2013**, *88*, 235203.
- (125) Perdew, J. P.; Ernzerhof, M.; Burke, K. Rationale for mixing exact exchange with density functional approximations. *J. Chem. Phys.* **1996**, *105*, 9982–9985.
- (126) Heyd, J.; Scuseria, G. E.; Ernzerhof, M. Hybrid functionals based on a screened Coulomb potential. *J. Chem. Phys.* **2003**, *118*, 8207–8215.
- (127) Cui, Z.-H.; Wang, Y.-C.; Zhang, M.-Y.; Xu, X.; Jiang, H. Doubly Screened Hybrid Functional: An Accurate First-Principles Approach for Both Narrow- and Wide-Gap Semiconductors. *J. Phys. Chem. Lett.* **2018**, *9*, 2338–2345.
- (128) Zhao, Y.; Truhlar, D. G. The M06 suite of density functionals for main group thermochemistry, thermochemical kinetics, noncovalent interactions, excited states, and transition elements: two new functionals and systematic testing of four M06-class functionals and 12 other functionals. *Theor. Chem. Acc.* **2008**, *120*, 215–241.
- (129) Zhang, M.-Y.; Jiang, H. Accurate Prediction of Band Structure of FeS₂: A Hard Quest of Advanced First-Principles Approaches. *Front. Chem.* **2021**, *9*, 747972.

- (130) Ennaoui, A.; Tributsch, H. Iron sulphide solar cells. *Sol. Cells* **1984**, *13*, 197–200.
- (131) Phung, Q. M.; Feldt, M.; Harvey, J. N.; Pierloot, K. Toward Highly Accurate Spin State Energetics in First-Row Transition Metal Complexes: A Combined CASPT2/CC Approach. *J. Chem. Theory Comput.* **2018**, *14*, 2446–2455.
- (132) Bajaj, A.; Janet, J. P.; Kulik, H. J. Communication: Recovering the flat-plane condition in electronic structure theory at semi-local DFT cost. *J. Chem. Phys.* **2017**, *147*, 191101.
- (133) Zaanen, J.; Sawatzky, G. A.; Allen, J. W. Band gaps and electronic structure of transition-metal compounds. *Phys. Rev. Lett.* **1985**, *55*, 418–421.
- (134) Sato, H.; Enoki, T.; Isobe, M.; Ueda, Y. Transport properties and magnetism of a helically Hund-coupled conductor: beta-MnO₂. *Phys. Rev. B* **2000**, *61*, 3563–3569.
- (135) Chevillot, J.-P.; Brenet, J. Influence d’ions étrangers sur la semi-conductibilité des bioxydes de manganèse. *C. R. Acad. Sci. Paris* **1959**, *278*, 776–778.
- (136) Druilhe, R. Nouveaux Semi-Conducteurs Magnetiques, Cristal-Lisant Dans La Structure Du Rutile. *C. R. Hebd. Séances Acad. Sci., Ser. B* **1966**, 653.
- (137) Kumar, N.; Sen, A.; Rajendran, K.; Rameshbabu, R.; Ragupathi, J.; Therese, H. A.; Maiyalagan, T. Morphology and phase tuning of alpha- and beta-MnO₂ nanocacti evolved at varying modes of acid count for their well-coordinated energy storage and visible-light-driven photocatalytic behaviour. *RSC Adv.* **2017**, *7*, 25041–25053.
- (138) Bigiani, L.; Gasparotto, A.; Maccato, C.; Sada, C.; Verbeeck, J.; Andreu, T.; Morante, J. R.; Barreca, D. Dual Improvement of beta-MnO₂ Oxygen Evolution Electrocatalysts via Combined Substrate Control and Surface Engineering. *ChemCatChem* **2020**, *12*, 5984–5992.

- (139) Franchini, C.; Podloucky, R.; Paier, J.; Marsman, M.; Kresse, G. Ground-state properties of multivalent manganese oxides: Density functional and hybrid density functional calculations. *Phys. Rev. B* **2007**, *75*, 195128.
- (140) Lim, J. S.; Saldana-Greco, D.; Rappe, A. M. Improved pseudopotential transferability for magnetic and electronic properties of binary manganese oxides from DFT+U+J calculations. *Phys. Rev. B* **2016**, *94*, 165151.
- (141) Bolzan, A.; Fong, C.; Kennedy, B.; Howard, C. Powder Neutron Diffraction Study of Pyrolusite, beta-MnO₂. *Aust. J. Chem.* **1993**, *46*, 939.
- (142) Huber, S. P.; Zoupanos, S.; Uhrin, M.; Talirz, L.; Kahle, L.; Häuselmann, R.; Gresch, D.; Müller, T.; Yakutovich, A. V.; Andersen, C. W.; Ramirez, F. F.; Adorf, C. S.; Gargiulo, F.; Kumbhar, S.; Passaro, E.; Johnston, C.; Merkys, A.; Cepellotti, A.; Mounet, N.; Marzari, N.; Kozinsky, B.; Pizzi, G. AiiDA 1.0, a Scalable Computational Infrastructure for Automated Reproducible Workflows and Data Provenance. *Sci. Data* **2020**, *7*, 300.
- (143) Uhrin, M.; Huber, S. P.; Yu, J.; Marzari, N.; Pizzi, G. Workflows in AiiDA: Engineering a high-throughput, event-based engine for robust and modular computational workflows. *Comput. Mater. Sci.* **2021**, *187*, 110086.
- (144) Himmetoglu, B.; Wentzcovitch, R. M.; Cococcioni, M. First-principles study of electronic and structural properties of CuO. *Phys. Rev. B* **2011**, *84*, 115108.
- (145) Mori-Sánchez, P.; Cohen, A. J.; Yang, W. Discontinuous Nature of the Exchange-Correlation Functional in Strongly Correlated Systems. *Phys. Rev. Lett.* **2009**, *102*, 066403.